Astronomy & Astrophysics

The GAPS programme with HARPS-N at TNG

XVI. Measurement of the Rossiter–McLaughlin effect of transiting planetary systems HAT-P-3, HAT-P-12, HAT-P-22, WASP-39, and WASP-60[*]

L. Mancini[1,3,4], M. Esposito[2], E. Covino[2], J. Southworth[5], K. Biazzo[6], I. Bruni[7], S. Ciceri[8], D. Evans[5], A. F. Lanza[6], E. Poretti[9], P. Sarkis[3], A. M. S. Smith[10], M. Brogi[11], L. Affer[12], S. Benatti[13], A. Bignamini[14], C. Boccato[13], A. S. Bonomo[4], F. Borsa[9], I. Carleo[13,15], R. Claudi[13], R. Cosentino[16], M. Damasso[4], S. Desidera[13], P. Giacobbe[4], E. González-Álvarez[12], R. Gratton[13], A. Harutyunyan[16], G. Leto[6], A. Maggio[12], L. Malavolta[13,15], J. Maldonado[12], A. Martinez-Fiorenzano[16], S. Masiero[12], G. Micela[12], E. Molinari[16,17], V. Nascimbeni[15,13], I. Pagano[6], M. Pedani[16], G. Piotto[15], M. Rainer[9], G. Scandariato[6], R. Smareglia[15], A. Sozzetti[4], G. Andreuzzi[16,18], and Th. Henning[3]

[1] Dipartimento di Fisica, Università di Roma Tor Vergata, Via della Ricerca Scientifica 1, 00133 Roma, Italy
    e-mail: lmancini@roma2.infn.it
[2] INAF – Osservatorio Astronomico di Capodimonte, via Moiariello, 16, 80131 Naples, Italy
[3] Max Planck Institute for Astronomy, Königstuhl 17, 69117 Heidelberg, Germany
[4] INAF – Osservatorio Astrofisico di Torino, via Osservatorio 20, 10025 Pino Torinese, Italy
[5] Astrophysics Group, Keele University, Keele ST5 5BG, UK
[6] INAF – Osservatorio Astrofisico di Catania, via S. Sofia 78, 95123 Catania, Italy
[7] INAF – Osservatorio Astronomico di Bologna, Via Ranzani 1, 40127 Bologna, Italy
[8] Department of Astronomy, Stockholm University, AlbaNova University Center, 106 91 Stockholm, Sweden
[9] INAF – Osservatorio Astronomico di Brera, via E. Bianchi 46, 23807 Merate (LC), Italy
[10] Institute of Planetary Research, German Aerospace Center, Rutherfordstrasse 2, 12489 Berlin, Germany
[11] Department of Physics, University of Warwick, Coventry CV4 7AL, UK
[12] INAF – Osservatorio Astronomico di Palermo, Piazza del Parlamento 1, 90134 Palermo, Italy
[13] INAF – Osservatorio Astronomico di Padova, Vicolo dell'Osservatorio 5, 35122 Padova, Italy
[14] INAF – Osservatorio Astronomico di Trieste, via G. B. Tiepolo 11, 34143 Trieste, Italy
[15] Dipartimento di Fisica e Astronomia G. Galilei, Università di Padova, Vicolo dell'Osservatorio 2, 35122 Padova, Italy
[16] INAF – Fundación Galileo Galilei, Rambla José Ana Fernandez Pérez 7, 38712 Breña Baja, Spain
[17] INAF – Osservatorio Astronomico di Cagliari, Via della Scienza 5, 09047 Selargius (CA), Italy
[18] INAF – Osservatorio Astronomico di Roma, via Frascati 33, 00040 Monte Porzio Catone (Roma), Italy

ABSTRACT

Context. The measurement of the orbital obliquity of hot Jupiters with different physical characteristics can provide clues to the mechanisms of migration and orbital evolution of this particular class of giant exoplanets.
Aims. We aim to derive the degree of alignment between planetary orbit and stellar spin angular momentum vectors and look for possible links with other orbital and fundamental physical parameters of the star-planet system. We focus on the characterisation of five transiting planetary systems (HAT-P-3, HAT-P-12, HAT-P-22, WASP-39, and WASP-60) and the determination of their sky-projected planet orbital obliquity through the measurement of the Rossiter–McLaughlin effect.
Methods. We used HARPS-N high-precision radial velocity measurements, gathered during transit events, to measure the Rossiter–McLaughlin effect in the target systems and determine the sky-projected angle between the planetary orbital plane and stellar equator. The characterisation of stellar atmospheric parameters was performed by exploiting the HARPS-N spectra, using line equivalent width ratios and spectral synthesis methods. Photometric parameters of the five transiting exoplanets were re-analysed through 17 new light curves, obtained with an array of medium-class telescopes, and other light curves from the literature. Survey-time-series photometric data were analysed for determining the rotation periods of the five stars and their spin inclination.
Results. From the analysis of the Rossiter–McLaughlin effect we derived a sky-projected obliquity of $\lambda = 21.2° \pm 8.7°$, $\lambda = -54°\,^{+41°}_{-13°}$, $\lambda = -2.1° \pm 3.0°$, $\lambda = 0° \pm 11°$, and $\lambda = -129° \pm 17°$ for HAT-P-3 b, HAT-P-12 b, HAT-P-22 b, WASP-39 b, and WASP-60 b, respectively. The latter value indicates that WASP-60 b is moving on a retrograde orbit. These values represent the first measurements of λ for the five exoplanetary systems under study. The stellar activity of HAT-P-22 indicates a rotation period of 28.7 ± 0.4 days, which allowed us to estimate the true misalignment angle of HAT-P-22 b, $\psi = 24° \pm 18°$. The revision of the physical parameters of the five exoplanetary systems returned values that are fully compatible with those existing in the literature. The exception to this is the WASP-60 system, for which, based on higher quality spectroscopic and photometric data, we found a more massive and younger star and a larger and hotter planet.

Key words. planetary systems – stars: late-type – stars: fundamental parameters – techniques: radial velocities – techniques: photometric

---

[*] Tables of the light curve and radial velocity data are only available at the CDS via anonymous ftp to cdsarc.u-strasbg.fr (130.79.128.5) or via http://cdsarc.u-strasbg.fr/viz-bin/qcat?J/A+A/613/A41

1. Introduction

The study of the physical and orbital properties of extrasolar planets, in connection with the physical characteristics of their host stars, provides important insight into formation and evolution mechanisms of planetary systems, which are currently a matter of extensive debated. In particular, the evolution theories of planetary orbits are very difficult to establish on solid ground because there are so many possible architectures of planetary systems and many factors can contribute to modify the dynamic of these systems during their secular life.

The existence of a hot-Jupiter population, i.e. Jupiter-mass planets with orbital periods of only a few days, is a clear indication that inward migration occurred during the process of formation or early evolution for many of these gaseous planets[1]. Widely accepted scenarios of the migration of giant planets, which are supported by hydrodynamic simulations, involve planet–disc interaction, in which planets are kept on circular orbits with orbital axes parallel to the stellar spin axis (e.g. Lin et al. 1996; Marzari & Nelson 2009; Bitsch & Kley 2011), whereas planets on eccentric and oblique orbits can be the result of planet–planet scattering (e.g. Rasio & Ford 1996; Chatterjee et al. 2008; Marzari 2014) or Kozai torque by a distant massive companion (e.g. Fabrycky & Tremaine 2007). Therefore, the orbital obliquity, ψ, i.e. the angle between the orbital angular momentum and the spin of the host star, represents an extremely important parameter, as we can use it to probe how planetary systems form and evolve. As all the above-mentioned migration scenarios probably occur (e.g. Nagasawa et al. 2008; Nelson et al. 2017), we must study a statistically significant sample of exoplanetary systems to quantify the relative importance of the orbital obliquity (Schlaufman 2010).

While ψ is a quantity that is difficult to determine, the measurement of its sky projection, λ, is commonly achievable for stars hosting transiting exoplanets, mainly through the observation of the Rossiter–McLaughlin (RM) effect. This is an anomalous radial velocity (RV) variation that occurs when a planet transits a rotating star and can be accurately measured for relatively bright stars with high-precision RV instruments. Precise values of λ have now been obtained for about a hundred giant exoplanets[2], the majority of which show values of λ close to zero similar to the planetary bodies orbiting our Sun, although a considerable fraction (nearly 40%) show substantial misalignment (Albrecht et al. 2012). Of these, ten are in nearly polar orbits and another ten are in retrograde orbits[3]. Such extreme spin–orbit misalignments may also be explained through secular mutual close encounters, or Kozai–Lidov oscillations of orbital eccentricity and inclination induced by a distant companion, whose orbit is significantly tilted with respect to the orbit of the inner planet (Nagasawa et al. 2008; Naoz et al. 2011).

As the number of the measurements of λ increased in recent years, several empirical trends were noted, of which the most debated is that between λ and the effective temperature, $T_{\rm eff}$,

of parent stars. By plotting these two quantities together, one can see that planetary systems having stars with $T_{\rm eff} \lesssim 6250\,{\rm K}$ have good spin–orbit alignment, whereas the values of λ for those with $T_{\rm eff} \gtrsim 6250\,{\rm K}$ are more broadly distributed (Winn et al. 2010; Albrecht et al. 2012). The suggestion that λ seems to increase as the amount of stellar surface convection decreases can be explained by the fact that tidal dissipation is much less efficient for hot stars than the cold stars because the former have a smaller convective zone than the latter (Valsecchi & Rasio 2014). However, the presence of several exceptions (e.g. WASP-8: Queloz et al. 2010; Bourrier et al. 2017; HAT-P-18: Esposito et al. 2014, HATS-14: Zhou et al. 2015) suggests that the truthfulness of the $\lambda - T_{\rm eff}$ trend has to be verified more accurately by enlarging the sample, especially by exploring the range of low values of $T_{\rm eff}$. This is a critical point because measurements of the RM effect become more arduous for slow-rotating cool stars and require large-aperture telescopes and spectrographs with high performances since the amplitude of the RM effect is $\propto k^2 v \sin i_\star$; k is the ratio of the planetary to stellar radii and $v \sin i_\star$ is the projected rotational velocity of the star.

Within the framework of the long-term observational programme Global Architecture of Planetary Systems (GAPS), which uses the high-resolution spectrograph HARPS-N at the 3.5 m Telescopio Nazionale Galileo (TNG), we conducted a sub-programme for studying the spin–orbit alignment of a large sample of known exoplanetary systems (Covino et al. 2013). Our project is especially focussed on those hosted by relatively cold stars, but still sufficiently bright ($V < 14\,{\rm mag}$) (Mancini et al. 2015; Esposito et al. 2017). Moreover, our programme is supported by photometric follow-up observations with an array of medium-class telescopes. We use these observations to record high-quality light curves of planetary-transit events of the targets in our sample list. The main aim is to refine the whole set of physical parameters of the planetary systems and check for possible stellar activity; starspots can actually play an important role in modelling transit light curves (e.g. Mancini et al. 2017). In this work, we present new detections of the RM effect for five exoplanetary systems for which measurements of λ were not available before now.

The paper is organised as follows. In Sect. 2 we briefly describe the systems that are the subjects of this study. Both spectroscopic and photometric observations are presented in Sect. 3, together with the description of the corresponding data reduction procedures. The analysis of the photometric light curves is discussed in Sect. 4. Section 5 is devoted to exploring possible stellar activity by analysing the survey-time-series photometric data. The stellar atmospheric properties and measurements of the spin–orbit relative orientation of the systems, based on HARPS-N data, are presented in Sect. 6. Our refinements of the physical parameters of the systems are reported in Sect. 7, with a particular attention to WASP-60, for which we found values different from those measured by its discoverers. Finally, in Sect. 8 we summarise and discuss the main results of this study.

2. Case history

In this work, we present measurements of the RM effect for five transiting exoplanetary systems. These systems are HAT-P-3, HAT-P-12, HAT-P-22, WASP-39, and WASP-60, each of which is composed of a hot giant planet, with an equilibrium temperature, $T_{\rm eq}$, in the range 960–1320 K, and a mid-K- or G-type star, with an effective temperature, $T_{\rm eff}$, in the range 4650–5900 K.

---

[1] Possible scenarios of in situ formation of hot Jupiters were also theorised (e.g. Bodenheimer et al. 2000; Boley et al. 2016; Batygin et al. 2016).

[2] Data taken from TEPCat: http://www.astro.keele.ac.uk/jkt/tepcat/rossiter.html (Southworth 2011).

[3] Following Addison et al. (2013), we have considered near-polar orbits as those with spin–orbit angles between $(3\pi/8) < \lambda < (5\pi/8)$ and $(-3\pi/8) > \lambda > (-5\pi/8)$ and retrograde orbits for spin–orbit angles between $(5\pi/8) \leq \lambda \leq (11\pi/8)$ and $(-5\pi/8) \geq \lambda \geq (-11\pi/8)$.

Their main physical parameters, which were also recalculated in this work (see Sect. 7), are summarised in the tables reported in Appendix C. The eccentricity of the orbits of each of the five exoplanet was fixed to zero, according to the values determined by Bonomo et al. (2017).

2.1. HAT-P-3

The planetary system HAT-P-3 is composed of a $V = 11.6$ mag metal-rich, early-K dwarf star, around which a hot Jupiter (mass $\approx 0.6 M_{\rm Jup}$ and radius $\approx 0.9 R_{\rm Jup}$) revolves on a circular orbit, producing transit events every 2.9 days with a depth of 1.5% (Torres et al. 2007). In recent years, several studies of this system were presented, reporting slightly improved values of the physical (Torres et al. 2008; Gibson et al. 2010; Chan et al. 2011; Southworth 2012; Torres et al. 2012; Eastman et al. 2013; Ricci et al. 2017) and orbital parameters (Torres et al. 2008; Madhusudhan & Winn 2009; Gibson et al. 2010; Nascimbeni et al. 2011; Chan et al. 2011; Pont et al. 2011; Sada et al. 2012; Southworth 2012; Eastman et al. 2013; Sada & Ramón-Fox 2016). Two occultations of HAT-P-3 b were measured with the *Spitzer* space telescope in the 3.6 and 4.5 μm bands, from which it was found that the planet has inefficient heat transfer from its day to night side, but it is not clear if there is a temperature inversion in its atmosphere (Todorov et al. 2013). No information is available about either its atmospheric composition or the obliquity of its orbit.

2.2. HAT-P-12

Having a mass of $\approx 0.2 M_{\rm Jup}$, HAT-P-12 b can be considered as a sub-Saturn type planet (Hartman et al. 2009). It moves on a circular orbit, transiting its parent star, a relatively metal-poor K4 V star, with a periodicity of 3.2 days and lowering its brightness by 2%. The orbital and physical parameters of this planetary system were revised by several authors (Lee et al. 2012; Knutson et al. 2014; Hinse et al. 2015; Mallonn et al. 2015; Sada & Ramón-Fox 2016) based on new photometric light curves. No occultations of HAT-P-12 b were detected so far (Todorov et al. 2013). The low density ($\approx 0.24 \rho_{\rm Jup}$) of the planet and relatively bright primary ($V = 12.8$ mag) make this system a suitable target for transmission spectroscopy. A near-infrared (NIR) transmission spectrum of the planet was presented by Line et al. (2013), based on data collected with the *Hubble* Space Telescope (HST); no water-absorption features were observed, suggesting an atmosphere dominated by high-altitude clouds. This result was confirmed by Mallonn et al. (2015), who extended the analysis to optical wavelengths via broadband photometric observations with a group of professional class telescopes.

2.3. HAT-P-22

The massive and compact hot Jupiter HAT-P-22 b (mass $\approx 2.1 M_{\rm Jup}$ and radius $\approx 1.1 R_{\rm Jup}$) circularly orbits a fairly metal-rich and bright ($V = 9.7$ mag) G5 V star with a period of 3.2 days, producing planetary-transit events with a depth of 1.5% (Bakos et al. 2011). Further studies of this planetary system, mostly based on new photometric light curves, presented slight refinements of the orbital (Knutson et al. 2014; Turner et al. 2016) and physical parameters (Torres et al. 2012; Hinse et al. 2015; Sousa et al. 2015; Baştürk et al. 2015; Turner et al. 2016). Occultation measurements of HAT-P-22 b with *Spitzer* were performed by Kilpatrick et al. (2017), who concluded that its atmosphere does not experience efficient recirculation.

2.4. WASP-39

The discovery of the transiting exoplanet WASP-39 b was announced by Faedi et al. (2011). It is a highly inflated Saturn-mass planet (mass $\approx 0.3 M_{\rm Jup}$ and radius $\approx 1.3 R_{\rm Jup}$) circularly orbiting a late G-type dwarf star with a period of roughly four days. Further observations refined the orbital (Ricci et al. 2015; Fischer et al. 2016; Maciejewski et al. 2016) and physical parameters (Maciejewski et al. 2016; Nikolov et al. 2016). Occultation measurements with *Spitzer* were also carried out for WASP-39 b, suggesting a very efficient circulation of energy from the day to the night side (Kammer et al. 2015). A Rayleigh scattering slope as well as sodium and potassium absorption features were detected by Fischer et al. (2016) using HST transit observations and complementary data from *Spitzer*. These findings were confirmed by ground-based, transmission-spectroscopy observations, which were obtained with the Very Large Telescope (VLT; Nikolov et al. 2016).

2.5. WASP-60

The hot Jupiter WASP-60 b was discovered by Hébrard et al. (2013), who measured for this planet a mass of $\approx 0.5 M_{\rm Jup}$ and a radius of $\approx 0.9 R_{\rm Jup}$. The authors found that it transits in front of its parent star, a G1 V star with $M_\star \approx 1.1 M_\odot$ and $R_\star \approx 1.1 R_\odot$, every ≈ 4.3 days, producing shallow transits of 0.6%. These measurements were based on RV data, photometric data from the SuperWASP survey, and on a single incomplete follow-up light curve. As we see in Sect. 7, several of these findings are not in agreement with the results presented in this work. According to Bonomo et al. (2017), the eccentricity of the orbit of WASP-60 b is compatible with zero, but with an uncertainty larger than 0.05. A new incomplete, photometric light curve of a WASP-60 b transit was reported by Turner et al. (2017). No further follow-up works have yet been presented for this exoplanetary system.

3. Observation and data reduction

In this section we present new times-series spectroscopic data of HAT-P-3, HAT-P-12, HAT-P-22, WASP-39, and WASP-60. The spectra were obtained with HARPS-N during their transit events with the specific purpose of measuring the RM effects for each of the five exoplanets. We also present new photometric follow-up observations of HAT-P-3, HAT-P-12, and WASP-60.

3.1. HARPS-N spectroscopic observations

The spectroscopic observations of the transits were carried out using the High Accuracy Radial velocity Planet Searcher-North (HARPS-N; Cosentino et al. 2012) spectrograph at the 3.58 m TNG on the following nights: 2013/06/10 (HAT-P-3), 2013/10/20 (WASP-60), 2014/04/03 (HAT-P-22), 2015/03/13 and 2015/04/24 (HAT-P-12), and 2015/05/04 (WASP-39). The observations were performed with a simultaneous Thorium-lamp spectrum for the stars with $V < 12$ (HAT-P-3 and HAT-P-22) and with fibre A on target and fibre B on sky for the other three fainter stars. The log of the HARPS-N observations is given in Table A.1.

The reduction of the spectra was performed using the latest version (3.7) of the HARPS-N data reduction software (DRS) pipeline (Cosentino et al. 2014; Smareglia et al. 2014). Radial velocity measurements, with corresponding uncertainties, were computed by cross-correlating each spectrum with a numerical template mask (Baranne et al. 1996; Pepe et al. 2002;
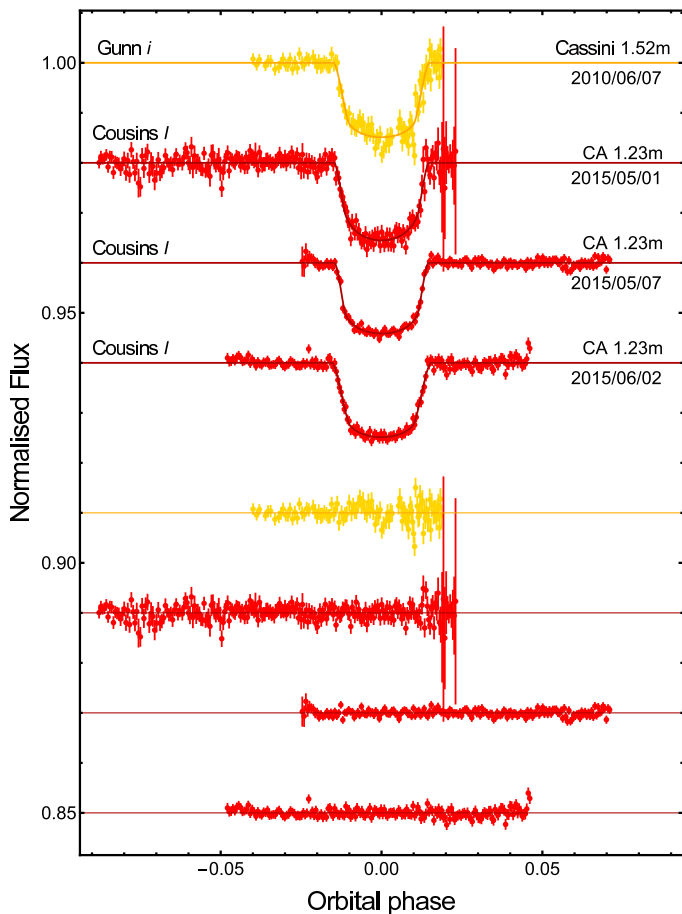
Fig. 1. Phased light curves of HAT-P-3 b transits presented in this work. These phased light curves are compared with the best JKTEBOP fits. The dates, telescopes, and filters related to the observation of each transit event are indicated. Residuals from the fits are plotted at the base of the figure.

Lovis & Pepe 2007). In addition to RVs, the DRS provides 1D wavelength-calibrated spectra, which we used for the determination of the atmospheric parameters of the star (see Sect. 6), the Mount Wilson S-index, and the $\log R'_{HK}$ chromospheric activity index for stars with $B-V < 1.2$ (Lovis et al. 2011). The RV measurements for our targets are reported in Tables B.1–B.5 for HAT-P-3, HAT-P-12, HAT-P-22, WASP-39, and WASP-60, respectively. The typical signal-to-noise ratio (S/N) of the extracted spectra is 31, 15, 61, 22, 26 per pixel at 550 nm for HAT-P-3, HAT-P-12, HAT-P-22, WASP-39, and WASP-60, respectively. We also checked that the RV measurements are not affected by the Moon. Following the method that was adopted by Esposito et al. (2017), a correction for Moon light contamination was applied by subtracting the cross-correlation function of fibre B from that of fibre A, and then measuring the stellar RV by means of a Gaussian fit to this difference. The values of the RV measurements obtained from this procedure are very similar to the previous measurements and, practically, within the uncertainties in all the five cases.

3.2. Photometric follow-up observations

Three of the planetary systems studied in this work were monitored with an array of medium-class telescopes with the purpose of obtaining high-quality light curves, which are extremely useful for refining the physical parameters and checking stellar

activity. These systems are HAT-P-3, HAT-P-12, and WASP-60; the telescopes used were the 2.5 m *Isaac Newton* Telescope (INT) in La Palma (Spain), the *Cassini* 1.52 m Telescope at the Astronomical Observatory of Bologna in Loiano (Italy), and the 2.2 m and 1.23 m telescopes at the German-Spanish Astronomical Centre at Calar Alto (Spain). As in previous observations with these telescopes (e.g. Mancini et al. 2013, 2015), the defocussing technique was adopted in all the observations to improve the quality of the photometric data significantly (Southworth et al. 2009). Telescopes were also autoguided and the corresponding CCDs were used unbinned. Sets of flat-fields frames were taken by observing blank fields during the sunset on the same nights as the transits. Together with bias frames, the flat fields were used to calibrate the scientific images during the data reduction phase (see Sect. 3.3). Details of each transit observation are reported in Table A.2.

3.2.1. Photometric follow-up observations of HAT-P-3

A complete transit of HAT-P-3 b was observed on June 2010 through a Gunn-i filter with the BFOSC (Bologna Faint Object Spectrograph & Camera) imager, which is mounted on the *Cassini* 1.52 m Telescope. The BFOSC is equipped with a back-illuminated CCD with 1300×1340 pixels and a pixel size of $20\,\mu$m. A focal reducer makes the telescope a f/5, implying a plate scale of 0.58 arcsec pixel^{-1} and a field of view (FOV) of 13 arcmin × 12.6 arcmin.

Three successive complete transits of HAT-P-3 b were observed between May and June 2015 using the Calar Alto (CA) Zeiss 1.23 m telescope. This telescope is equipped with the DLR-MKIII camera, which has 4000×4000 pixels of $15\,\mu$m size. The plate scale is 0.32 arcsec pixel^{-1}, which gives an FOV of 21.5 arcmin × 21.5 arcmin. All the three transits were observed using a Cousins-I filter.

3.2.2. Photometric follow-up observations of HAT-P-12

A partial transit of HAT-P-12 b was observed at the end of April 2010 using the wide field camera (WFC) at the prime focus of the INT 2.5 m telescope. WFC consists of four thinned EEV 2k × 4k CCDs, which have a pixel size of $13.5\,\mu$m corresponding to 0.33 arcsec pixel^{-1}. A complete transit was observed few nights later using the CA 2.2 m telescope and the multi-band imager BUSCA. This instrument is equipped with dichroics, which split the incoming starlight towards four Loral CCD4855 cameras (4000×4000 pixels of $15\,\mu$m size), allowing simultaneous broadband, four-band transit photometry in the optical window (Southworth et al. 2012; Mancini et al. 2014; Ciceri et al. 2015). For this transit, we chose to have Strömgren-u filter in the bluest arm, Gunn-g and r filters at intermediate bands, and Johnson I in the reddest arm.

Another partial transit was observed through a Gunn-r filter with the *Cassini* telescope on April 2012. By using the CA 1.23 m telescope we observed other six (five complete and one partial) transit events of HAT-P-12 b. These observations were performed between 2012 and 2016 using Cousins-R (four times) and I (two times) filters.

3.2.3. Photometric follow-up observations of WASP-60

A transit of WASP-60 b was observed on October 2014 through a Cousins-I filter with the CA 1.23 m telescope. To our knowledge, this is the only complete follow-up transit event that was ever observed for this target.
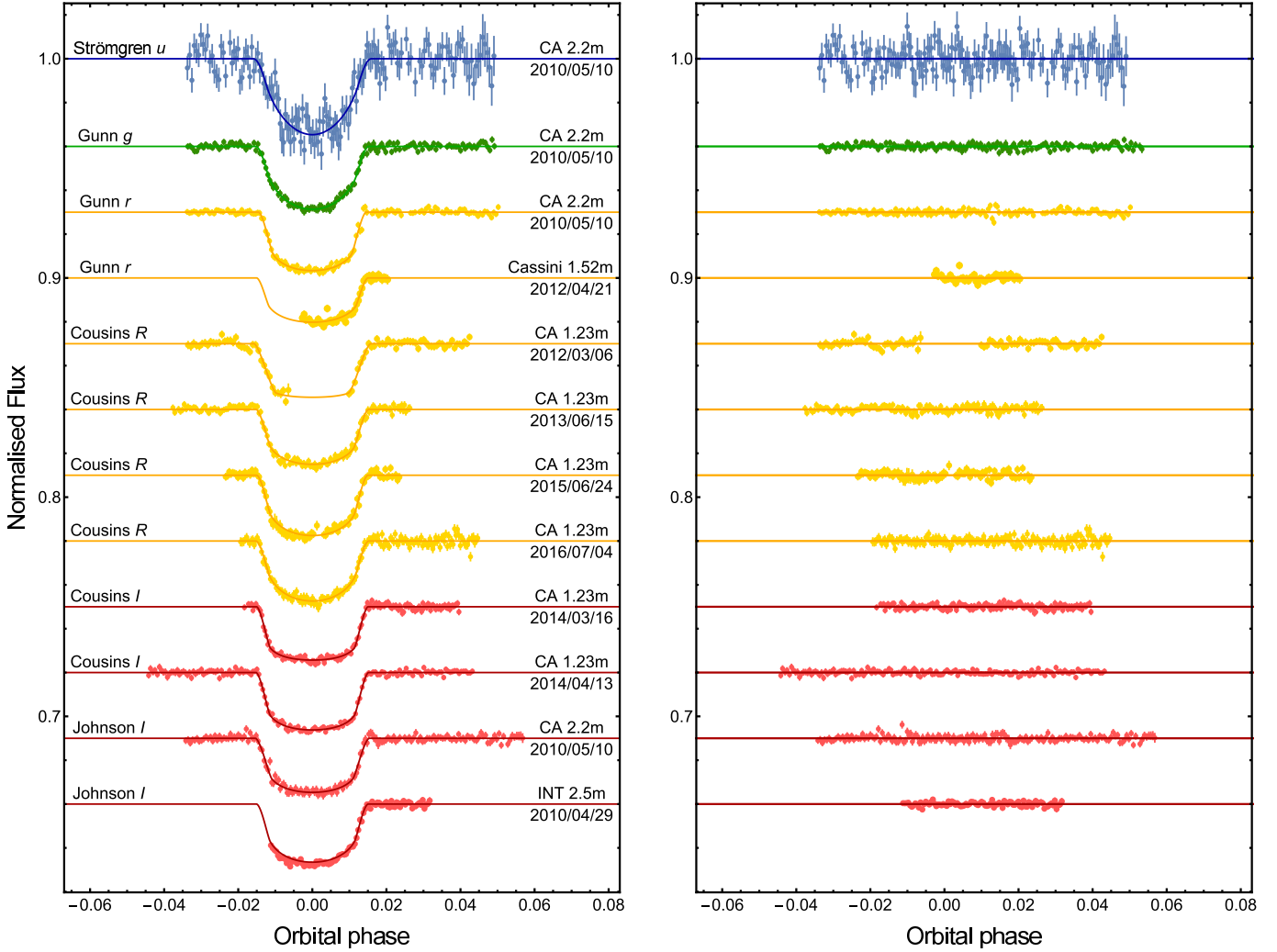
Fig. 2. Phased light curves of HAT-P-12 b transits presented in this work. These phased light curves are ordered based on the filter used and compared with the best JKTEBOP fits. The dates, telescopes, and filters related to the observation of each transit event are indicated. Residuals from the fits are plotted in the *right-hand panel*.

3.3. Reduction of the photometric data

The photometric data were reduced using a modified version of the DEFOT pipeline. This is written in IDL[4] and described by Southworth et al. (2014). Briefly summarising the procedure, we made a median combination of all the calibration images to create master-bias and master-flat frames, and we used these to correct the scientific images. We then identified the target and a suitable set of non-variable stars in each scientific image. We placed three apertures around the stars with radii chosen based on the lowest scatter achieved when compared with a fitted model. Pointing variations of the stars were also corrected with respect to a reference image by re-centring the apertures. The non-variable stars were used as reference stars to extract the photometry of the target using the APER routine[5]. Light curves were created for each transit data set with a first or a second-order polynomial fitted to the out-of-transit data. We simultaneously fit the comparison-star weights and polynomial coefficients to minimise the scatter outside the transit. The final light curves are plotted in Figs. 1, 2, and 5.

---

[4] The acronym IDL stands for Interactive Data Language and is a trademark of Harris Geospatial Solutions.
[5] APER is part of the ASTROLIB subroutine library distributed by NASA.

4. Light-curve analysis

The light curves of the transit events of HAT-P-3, HAT-P-12, and WASP-60, which were presented in the previous section, were individually studied with the JKTEBOP code (Southworth 2013) to find the best-fitting model for each of these events.

For HAT-P-3, we also considered the JKTEBOP best-fitting results obtained by Southworth (2012), who analysed five published light curves of HAT-P-3 b transits; moreover, for WASP-60, we considered the partial light curve obtained by Turner et al. (2017) and modelled this event with JKTEBOP as well (see Fig. 5).

For the other two systems, HAT-P-22 and WASP-39, we collected all the light curves available from the literature and modelled each one of these with JKTEBOP as well. For HAT-P-22 we used the light curves from Bakos et al. (2011), Baştürk et al. (2015), Hinse et al. (2015), and Turner et al. (2016); while for WASP-39 we used those from Faedi et al. (2011), Ricci et al. (2015), and Maciejewski et al. (2016). These light curves are shown in Figs. 3 and 4, in which the telescopes and the filters used are also specified.

The JKTEBOP code represents the star and planet as spheres and uses the Levenberg-Marquardt optimisation algorithm to fit the parameters of the light curves. The main parameters to be

Table 1. Final photometric parameters for the five exoplanetary systems analysed in this work.

System	Orbital period (day)	Time of mid-transit (BJD−2400000)	Orbital inclination, i (°)	$r_\star + r_p$	$r_p/r_\star$
HAT-P-3[a]	2.89973838 (27)	57150.39472 (58)	86.31 ± 0.19	0.11317 ± 0.00180	0.11056 ± 0.00068
HAT-P-12[b]	3.21305992 (35)	55328.49068 (19)	89.10 ± 0.24	0.09549 ± 0.00095	0.13898 ± 0.00069
HAT-P-22[c]	3.21223328 (58)	54930.22016 (16)	86.46 ± 0.41	0.13107 ± 0.00354	0.10911 ± 0.00065
WASP-39[d]	4.0552941 (34)	55342.96913 (63)	87.32 ± 0.17	0.10303 ± 0.00156	0.14052 ± 0.00077
WASP-60[e]	4.3050040 (59)	56952.43264 (17)	86.05 ± 0.57	0.12795 ± 0.00609	0.08986 ± 0.00009

Notes. The parameters $r_\star$ and r_p are the fractional stellar and planetary radius, respectively. The quantities in brackets denote the uncertainty in the final digit of the preceding number. [a]The photometric parameters of HAT-P-3 were estimated from the light curves presented in this work (Fig. 1), incorporating results from Southworth (2012) (see text). [b]The photometric parameters of HAT-P-12 were estimated from the light curves presented in this work, see Fig. 2. [c]The photometric parameters of HAT-P-22 were estimated from the light curves taken from various works (Bakos et al. 2011; Baştürk et al. 2015; Hinse et al. 2015; Turner et al. 2016), see Fig. 3. [d]The photometric parameters of WASP-39 were estimated from the light curves taken from different works (Faedi et al. 2011; Ricci et al. 2015; Maciejewski et al. 2016), see Fig. 4. [e]The photometric parameters of WASP-60 were estimated from the light curve presented in this work and the one from Turner et al. (2017), see Fig. 5.
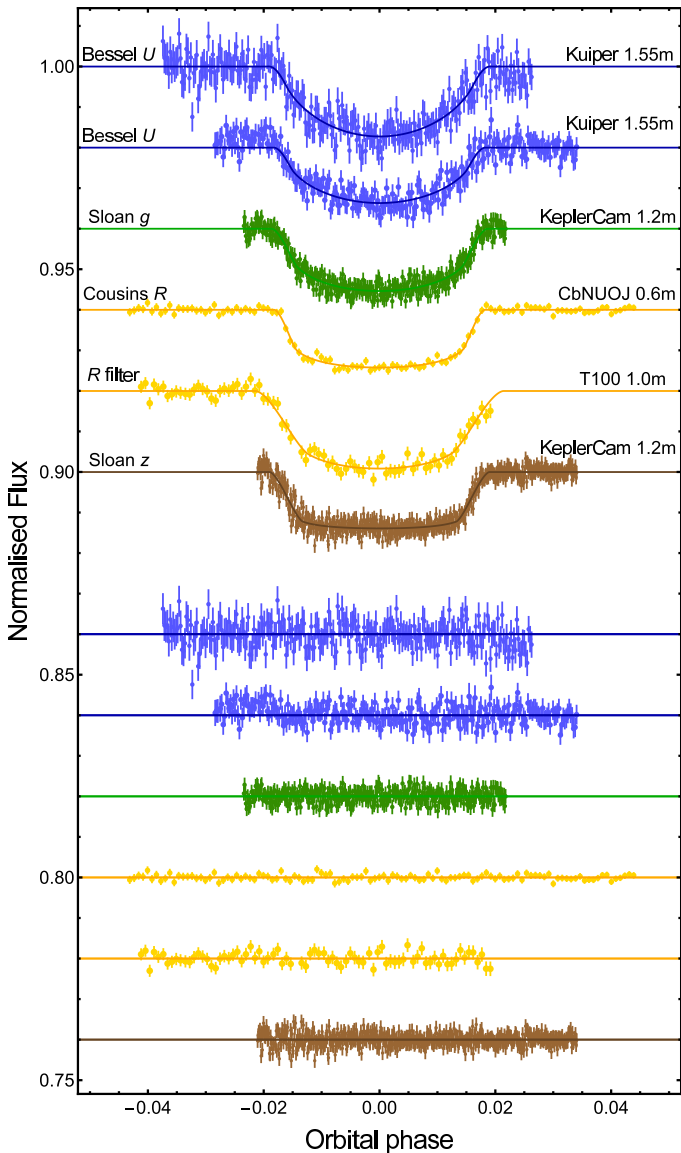

Fig. 3. Phased light curves of HAT-P-22 b transits taken from the literature. These phased light curves are compared with the best JKTEBOP fits. The telescopes and filters related to the observation of each transit event are indicated. Residuals from the fits are plotted at the base of the figure.

fitted are the orbital period and inclination (P and i), time of transit midpoint (T_0), and sum and ratio of the fractional radii, which are defined as $r_\star = R_\star/a$ and $r_p = R_p/a$, where $R_\star$ and R_p are the true radii of the star and planet, and a is the semi-major axis of the planetary orbit. We used a quadratic law to describe the effect of the limb darkening (LD) of the star and fitted the LD coefficients with JKTEBOP, taking into account the differences between the properties of the various stars and filters used. The orbital eccentricity was fixed to zero for all the systems, based on the results of Bonomo et al. (2017). Since time-series photometry is generally affected by correlated (red) noise (Carter & Winn 2009), which is not taken into account by the APER routine, we inflated the error bars of the photometric measurements to give a reduced χ^2 of $\chi^2_\nu = 1$ during the best-fitting process of each light curve. The light curves and corresponding JKTEBOP best-fitting lines are reported in Figs. 1–5 for HAT-P-3, HAT-P-12, HAT-P-22, WASP-39, and WASP-60, respectively.

The uncertainties of the fitted parameters were also estimated with JKTEBOP, by running both a Monte Carlo and a residual-permutation algorithm. For each light curve, we ran at least 10 000 simulations for the Monte Carlo algorithm, and the maximum number of simulations (i.e. one less than the number of datapoints) for the residual-permutation algorithm, and adopted the largest of the two 1σ values as the final uncertainty for each parameter. The final values of each parameter were finally estimated by means of a weighted average of the values extracted from the fit of all the individual light curves, using the relative uncertainties as a weight, and these values are reported in Table 1. The orbital ephemerides are also shown, as they were recalculated performing a weighted linear least-squares fit to all the mid-transit times vs. their cycle number. For this task, we considered all the light curves that were discussed above and the times of mid-transit from the discovery papers.

5. Frequency analysis of the time-series light curves

Time-series photometric data are available in the WASP[6] and HAT[7] databases for the five stars included in this study. These data are very dense (thousands of measurements) and span a long time baseline (hundreds of days). They can be useful for detecting any periodic or quasi-periodic signal, which could

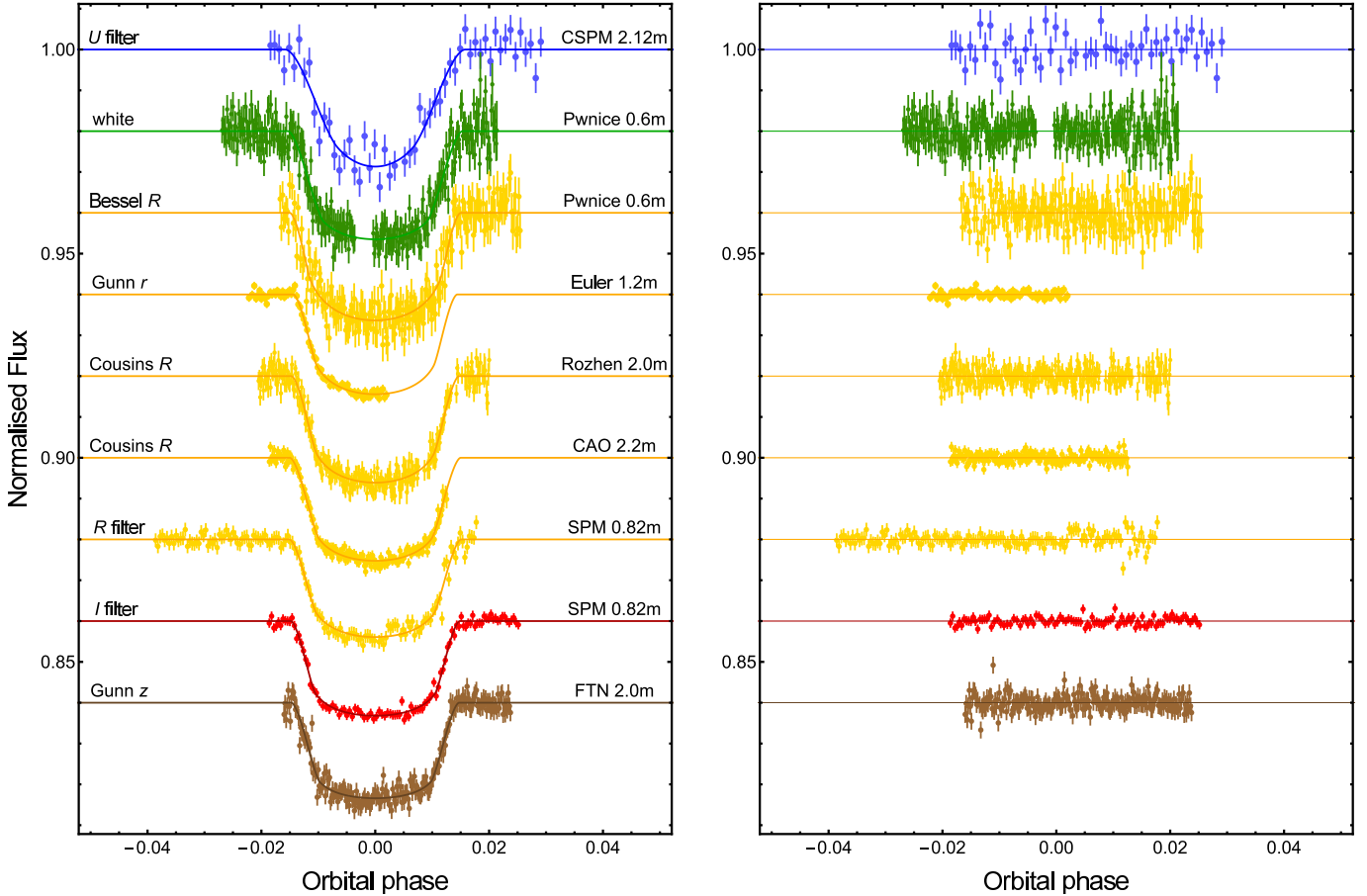[6] https://exoplanetarchive.ipac.caltech.edu
[7] https://hatnet.org

Fig. 4. Phased light curves of WASP-39 b transits taken from the literature. These phased light curves are compared with the best JKTEBOP fits. The telescopes and filters related to the observation of each transit event are indicated. Residuals from the fits are plotted in the *right-hand panel*.
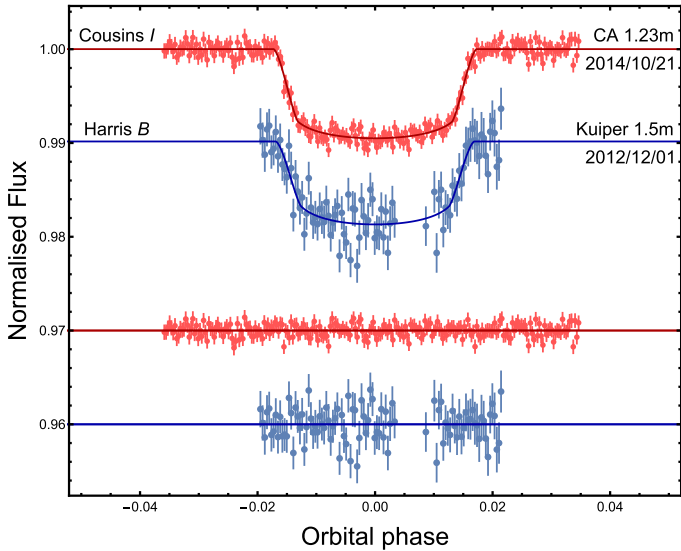

Fig. 5. *Top light curve*: phased light curve of the WASP-60 b transit presented in this work. *Bottom light curve*: phased light curve of a WASP-60 b transit observed by Turner et al. (2017). The dates, telescopes, and filters related to the observation of these two transit events are indicated. Both light curves are compared with the best JKTEBOP fits and the corresponding residuals are plotted at the base of the figure.

indicate stellar activity and hence allow us to suggest a rotational period for some of the five stars. We used the iterative sine-wave least-squares method (Vaniĉek 1971) to perform the frequency

analysis. We also obtained amplitude spectra and we determined the mean level noise in the 0.01–0.90 d^{-1} frequency interval. We then computed the S/N of each peak to infer the significance by assuming a threshold of 4.0 (Kuschnig et al. 1997).

5.1. Stars without a clear signal: WASP-60, HAT-P-12, WASP-39

The frequency analysis of the WASP-60 time series did not detect any peak. The mean level of the noise is 0.29 mmag.

The analysis of the data collected on HAT-P-12 does not suggest a clear value for the rotational frequency, although some structures of peaks can be occasionally seen in the spectra obtained from the different photometry provided. The noise level of the HAT-P-12 measurements is 0.89 mmag and this hampers the clear identification of the rotational signals, if any.

The frequency spectrum of the time series on WASP-39 shows a peak that is close to the frequency corresponding to the synodic month. On the basis of the photometric data only, we conservatively interpret such a peak as spurious, since WASP-39 is an equatorial star and hence moonlight can alter the measurements in an almost regular way.

5.2. Stars with a signal: HAT-P-3, HAT-P-22

The original time series of HAT-P-3 is very noisy and characterised by a dense group of outliers. By removing these outliers, we obtained a less scattered data set showing a noise level of 1.1 mmag. The frequency analysis reveals a peak at 0.054 d^{-1},
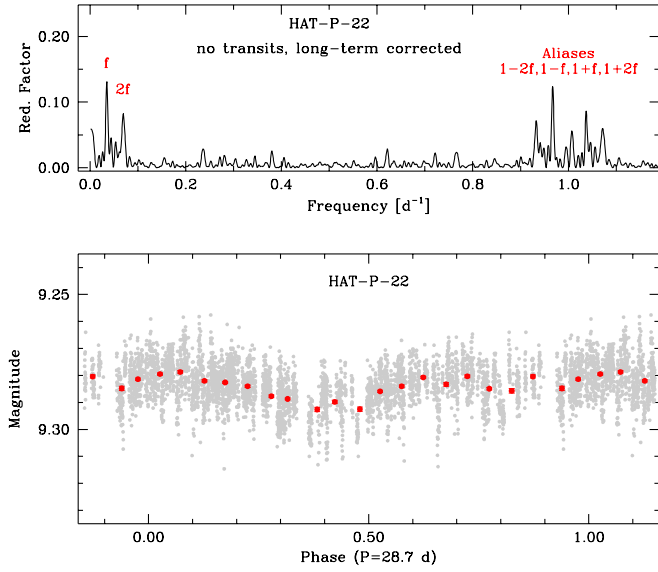
Fig. 6. Detection of the rotational period of HAT-P-22. *Top*: power spectrum of the photometric measurements. The peaks corresponding to $f = 0.0345$ d^{-1}, $2f$, and their aliases are indicated. *Bottom*: photometric measurements (in grey) folded with $P = 28.7$ d. The error bars of the mean values of the binned data (red circles) have the same size of the points.

corresponding to 18.5014 d. The amplitude is 3.8 mmag, putting the $S/N = 3.4$ detection below the significance level.

The case of HAT-P-22 is by far the most interesting. The preliminary periodogram showed a peak at a very low frequency, which is produced by a long-term trend in the time series. We corrected it by subtracting a linear best fit and recomputed the periodogram. In such a way, we could clearly detect two peaks at 0.0345 and 0.0690 d^{-1} (Fig. 6, top panel). These two peaks are not related to any peak in the spectral window of the data. The second frequency is twice the first. The amplitude of this signal is 5.6 mmag, that of the noise is 0.8 mmag only ($S/N = 7.1$, largely significant). We note that $f = 0.0345$ d^{-1} is still a frequency close to that corresponding to the synodic month, but unlike WASP-39, HAT-P-22 is a high-declination star and the signal shows a larger amplitude and a highly non-sinusoidal shape. Therefore, we are keen to interpret such detections as a clear hint of a flux modulation over a rotational period close to 29 d (corresponding to $f = 0.0345$ d^{-1}), shaped like a double wave by the harmonic $2f$ (Fig. 6, bottom panel). The low-frequency peak can be ascribed by long-term variations of the surface features, due to a much longer stellar activity cycle. We refined the value of the rotational period using the MTRAP code (Carpino et al. 1987), allowing the simultaneous fit with $f, 2f$, and the low-frequency component, thus obtaining $P_{rot} = 28.7 \pm 0.4$ d.

6. HARPS-N spectra analysis

6.1. Stellar atmospheric parameters

We used the HARPS-N spectra to perform a detailed spectroscopic characterisation of the host-star atmospheric parameters, i.e. effective temperature T_{eff}, surface gravity $\log g$, iron abundance [Fe/H], and projected rotational velocity $v \sin i_\star$, where $i_\star$ is the inclination of the stellar rotation axis with respect to the line of sight. To this purpose, for each target we obtained a single, high S/N, 1D spectrum by averaging all the spectra available,

Table 2. Stellar atmospheric parameters determined from HARPS-N spectra.

Object	T_{eff} (K)	$\log g$ (dex)	[Fe/H]	$v \sin i_\star$ (km s^{-1})
HAT-P-3	5190 ± 80	4.58 ± 0.10	$+0.24 \pm 0.08$	1.4 ± 0.5
HAT-P-12	4665 ± 50	4.55 ± 0.21	-0.20 ± 0.09	0.5 ± 0.5
HAT-P-22	5314 ± 50	4.39 ± 0.16	$+0.30 \pm 0.09$	1.3 ± 0.7
WASP-39	5485 ± 50	4.41 ± 0.15	$+0.01 \pm 0.09$	1.0 ± 0.5
WASP-60	6105 ± 50	4.31 ± 0.11	$+0.26 \pm 0.07$	3.8 ± 0.6

after correcting each one spectrum for the corresponding RV shift; these spectra, acquired during bright-time, were corrected for moonlight contamination by subtracting the sky-background estimated from fibre B, as described in Sect. 3.1.

Preliminary estimates of the effective temperature for the five targets were obtained by applying the method of equivalent width (EW) ratios of photospheric absorption lines, making use of the ARES[8] automatic code (Sousa et al. 2007) and the calibration for FGK dwarf stars by Sousa et al. (2010). The atmospheric stellar parameters, T_{eff}, $\log g$, and [Fe/H] were then derived via the program MOOG (Sneden 1973; version 2013) and EW measurements of iron lines, as described in detail by Biazzo et al. (2012, and references therein). The projected rotational velocity was estimated with the same code and applying the spectral synthesis method (D'Orazi et al. 2011). The results are reported in Table 2 and are in good agreement with previous estimates, with the exception of WASP-60, for which we measured a slightly hotter temperature and a higher iron abundance (see Sect. 7).

6.2. Stellar activity indexes

The average spectra were also used to analyse the Ca II H&K lines and measure both the chromospheric Mount Wilson S-index and $\log R'_{HK}$ index for each of the five stars; see Table 3. In particular the $\log R'_{HK}$ indexes indicate low activity in all the cases, confirming the general non-detections of the rotational periods in the photometric data (see Sect. 5). Adopting the calibration scales by Noyes et al. (1984) and Mamajek & Hillenbrand (2008), the level of the stellar activity provides an indication of how fast the stars rotate and how old they are. The projected rotation velocity and age estimated in this way are also reported in Table 3. We note that the predicted P_{rot} for HAT-P-22 (48–52 d) seems too long with respect to that determined from photometric data (28.7 d). Also the values of P_{rot} for HAT-P-12 and WASP-39 are not those expected for mid/late K-dwarf stars (McQuillan et al. 2014). On the other hand, the predicted P_{rot} for HAT-P-3 (20 d) is in good agreement with the value suspected from photometry (18.5 d).

6.3. Determination of the spin–orbit alignment

The analysis of the HARPS-N RV data, for measuring the orbital obliquity of the five planetary systems, was performed using a code developed by our team, which was already used for this purpose in the previous works of the series. The most recent work, Esposito et al. (2017), provides a detailed description of the RM-effect modelling and the fitting algorithm.

We used the transit-bracketing RV time series to derive the best-fitting values for three parameters: the sky-projected orbital

---

[8] http://www.astro.up.pt/~sousasag/ares/

Table 3. Stellar activity indexes and related parameters.

Object	S-index	$B - V$	$\log R'_{HK}$	P_{rot}^a (day)	P_{rot}^b (day)	Age^c (Gyr)
HAT-P-3	0.217 ± 0.016	0.67	-4.75 ± 0.06	20.2 ± 2.0	19.6 ± 2.3	2.6 ± 0.6
HAT-P-12^d	0.364 ± 0.054 0.375 ± 0.075	1.09	-4.88 ± 0.07 -4.87 ± 0.09	43.9 ± 3.7 43.3 ± 5.0	44.5 ± 4.9 43.9 ± 6.5	5.5 ± 1.1 5.3 ± 1.4
HAT-P-22	0.154 ± 0.004	0.86	-5.09 ± 0.02	48.1 ± 0.8	52.6 ± 1.1	9.6 ± 0.4
WASP-39	0.183 ± 0.017	0.84	-4.97 ± 0.06	42.1 ± 2.6	44.0 ± 3.9	7.2 ± 1.1
WASP-60	0.146 ± 0.009	0.68	-5.10 ± 0.07	31.8 ± 1.9	34.8 ± 2.7	6.84 ± 0.93

Notes. [a] This value was obtained adopting Noyes et al. (1984) calibration scale. [b] This value was obtained adopting Mamajek & Hillenbrand (2008) calibration scale. [c] This value was obtained adopting Mamajek & Hillenbrand (2008) calibration scale. [d] The top values refer to the transit observed on 2015.03.14, while the bottom values to the transit observed on 2015.04.24.

Table 4. Parameters from the best-fitting models of the RM effect for the five planetary systems.

Object	λ (°)	$v \sin i_\star$ (km s^{-1})	γ (km s^{-1})	ΔBIC
HAT-P-3	21.2 ± 8.7	1.20 ± 0.36	-23.3849 ± 0.0007	33.5
HAT-P-12	-54^{+41}_{-13}	$0.99^{+0.42}_{-0.46}$	-40.4589 ± 0.0023	10.3
HAT-P-22	-2.1 ± 3.0	1.65 ± 0.26	12.6370 ± 0.0004	71.4
WASP-39	0 ± 11	1.40 ± 0.25	-58.4421 ± 0.0020	19.7
WASP-60	-129 ± 17	2.97 ± 0.47	-26.5323 ± 0.0021	19.3

Notes. The ΔBIC values, i.e. the difference between the BIC values calculated from the best-fitting models with and without the RM effect, are also shown.

obliquity angle λ, the stellar projected rotational velocity $v \sin i_\star$, and the systemic RV γ. All the other relevant parameters were kept fixed to the values obtained by the photometric and spectroscopic data analysis, and their uncertainties were propagated in the determination of the error bars for λ, $v \sin i_\star$, and γ. The final results are reported in Table 4, while the best-fitting RV models are shown in Figs. 7 and 8, superimposed on the data sets. We found that HAT-P-22 and WASP-39 are planetary systems with well-aligned orbits ($\lambda = -2.1° \pm 3.0°$ and $\lambda = 0° \pm 11°$, respectively); the orbit of HAT-P-3 b is slightly misaligned ($\lambda = 21.2° \pm 8.7°$); concerning HAT-P-12 b, our results also indicate a very misaligned orbit, however this is not well constrained ($\lambda = -54°^{+41°}_{-13°}$); finally, WASP-60 b clearly shows a retrograde orbit ($\lambda = -129° \pm 17°$), Fig. 8.

Considering the small amplitudes of the RM effects and the accuracy of our RV measurements, we used the Bayesian information criterion (BIC) to perform a statistical comparison of our best-fitting results with those without RM effect. The BIC value was calculated for each data set using the corresponding number of data points, for both cases, i.e. with and without RM (the number of parameters estimated from the model was 3 for the fit with the RM effect and 1 for the fit with no RM effect). The differences in BIC are reported in Table 4 and they strongly support, in all cases, the statistical significance of the detection of the RM effect.

Knowing the rotational period of HAT-P-22 ($P_{rot} = 28.7 \pm 0.4$ d; see Sect. 5), we used the following formula:

$$P_{rot} \approx \frac{2\pi R_\star}{v \sin i_\star} \sin i_\star, \tag{1}$$

to estimate the angle $i_\star$, which resulted to be $62° \pm 19.0°$. Then, we can simply estimate the true misalignment angle by using Eq. (7) in Winn et al. (2007), i.e.

$$\cos \psi = \cos i_\star \cos i + \sin i_\star \sin i \cos \lambda, \tag{2}$$

thus obtaining $\psi = 25° \pm 18°$.

7. Physical parameters

Based on the data described in the previous sections, we reviewed the physical properties of the planetary systems HAT-P-3, HAT-P-12, HAT-P-22, WASP-39, and WASP-60. For this purpose, we followed the homogeneous studies approach (see Southworth 2012 and references therein) and combined the measured parameters from the light curves and spectroscopic observations with constraints on the properties of the host stars coming from theoretical stellar evolutionary models.

The spectroscopic properties of the host stars that we used are the effective temperature T_{eff}, the logarithmic surface gravity $\log g$, iron abundance, and projected rotational velocity $v \sin i_\star$. These values were obtained from the analysis of the HARPS-N spectra, Sect. 6.

Since most of the HARPS-N data were collected during transit events, we do not have enough out-of-transit RV points for a precise estimation of the velocity amplitude, K_A, of the RV curves, hence we adopted the values from the literature (see Tables C.2–C.5). The only exception was the case of HAT-P-3, for which we measured K_A using out-of-transit RV HIRES + HARPS-N data.

Having established a good set of input parameters, we used the JKTABSDIM code (Southworth 2009) to redetermine the main physical properties of the five planetary systems. The JKTABSDIM code maximises the agreement between the measured $R_\star/a$ and T_{eff} with those predicted by a set of five theoretical models by iteratively modifying the velocity amplitude of the planet. The code also considers a wide range of possible ages for each of the host stars and, at the end, returns five different estimates for each of the output parameters. We took the unweighted means as the final values of the parameters. Statistical uncertainties were propagated from the error bars in the values of all input parameters, whereas systematic uncertainties were calculated based on the maximum deviation between the values of the final parameters and individual values coming from the five theoretical models. Our final values are reported in Tables C.1–C.5, and compared with values taken from the literature.
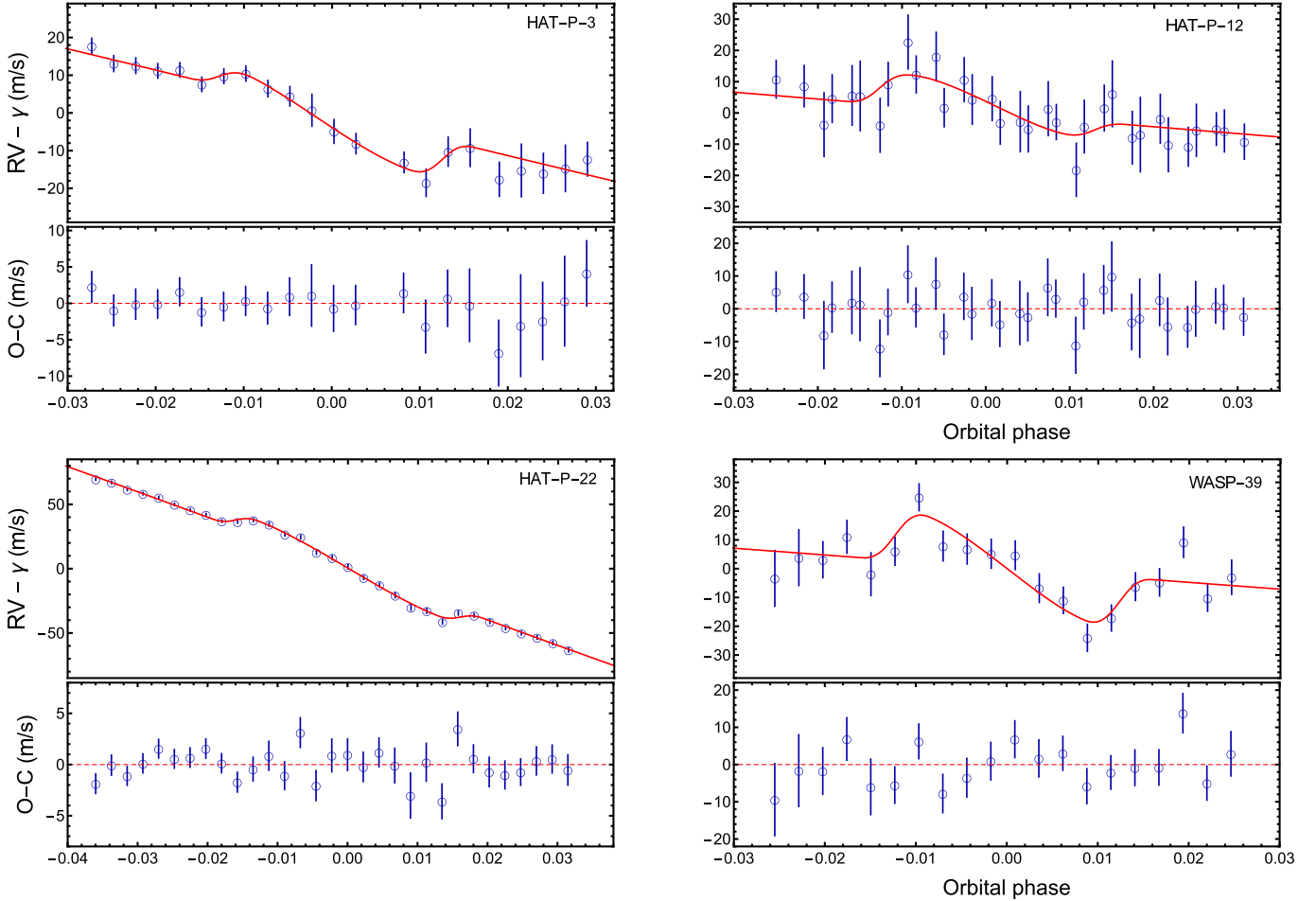
Fig. 7. Phase-folded RV data of HAT-P-3, HAT-P-12, HAT-P-22, and WASP-39 taken with HARPS-N during planetary-transit events. Superimposed are the best-fitting RV-curve models. The corresponding residuals are plotted in the *bottom panels*.
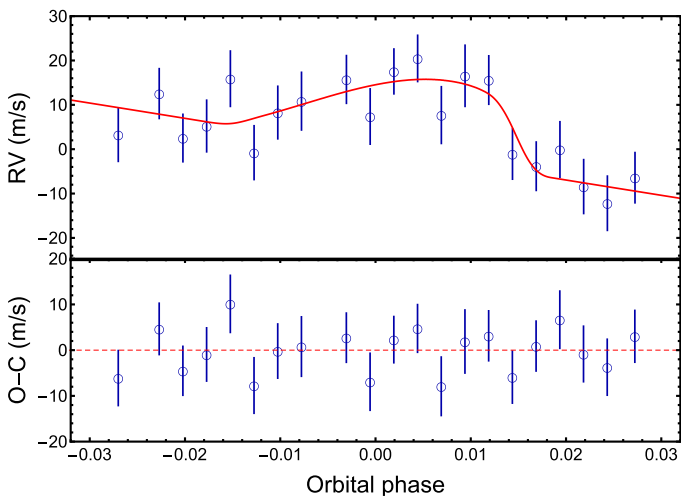

Fig. 8. Phase-folded RV data of WASP-60 taken with HARPS-N during a planetary-transit event. Superimposed is the best-fitting RV-curve model. The corresponding residuals are plotted in the *bottom panel*.

For HAT-P-3, HAT-P-12, HAT-P-22, and WASP-39, we found that our measured radii and masses for the stars and planets were all within the error bars of literature determinations. Our results are therefore in good agreement with previous works.

7.1. Lower density for WASP-60 b

For WASP-60 we obtained significantly different physical parameters with smaller error bars than in the literature (see Table C.5). Firstly, we measured a smaller stellar density than in Hébrard et al. (2013). The latter was based on sparse follow-up photometry. Secondly, based on HARPS-N data, we estimated a higher stellar temperature, i.e. 6105 ± 50 K vs. 5900 ± 100 K, which changes the spectral type from G1 V to F9 V. Therefore, we found that the WASP-60 is a younger and more massive star than was thought. Moreover, we found that the planet WASP-60 b is larger ($R_{\rm p} = 1.225 \pm 0.069\, R_{\rm Jup}$ vs. $R_{\rm p} = 0.86 \pm 0.12\, R_{\rm Jup}$), much less dense ($\rho_{\rm p} = 0.285 \pm 0.052\, \rho_{\rm Jup}$ vs. $\rho_{\rm p} = 0.8 \pm 0.3\, \rho_{\rm Jup}$), has a smaller surface gravity ($g_{\rm p} = 9.2 \pm 1.2\, {\rm m\,s}^{-2}$ vs. $g_{\rm p} = 15.5^{+4.9}_{-3.7}\, {\rm m\,s}^{-2}$) and is hotter ($T_{\rm eq} = 1479 \pm 35$ K vs. $T_{\rm eq} = 1320 \pm 75$) than that was measured by Hébrard et al. (2013).

We stress that, in obtaining these results, we used spectroscopic data of higher quality with respect to those used by Hébrard et al. (2013). Furthermore, for the analysis of the photometric parameters, we used two light curves: the one presented in Sect. 3.2.3 and the one from Turner et al. (2017). Comparing the quality of these two light curves (see Fig. 5), we note that the light curve obtained with the CA 1.23 m telescope has a longer coverage of the baseline (before the ingress and after the egress) and its points are much less scattered and have smaller uncertainties. Therefore, the analysis of the photometric parameters is

dominated by the CA light curve, which allowed us to obtain more precise measurements of the contact points and transit depth.

Figure 9 shows the change in position in the planet mass-radius diagram (top panel) and planet mass–density diagram (bottom panel). The revised positions are indicated with green points, while red points indicate the previous values from Hébrard et al. (2013). The values of the other transiting exoplanets were taken from the TEPCat catalogue[9]. For illustration, the bottom panel of Fig. 9 shows 1 Gyr isochrones of exoplanets at 0.045 au orbital separation from a solar analogue (Fortney et al. 2007), suggesting that the mass of the core of WASP-60 b should be extremely small.

7.2. Timescales of tidal evolution

All the systems considered in this investigation are likely not synchronised and their total angular momentum is between 0.52 and 0.63 of the minimum critical angular momentum that allows a binary system to reach a stable equilibrium during its tidal evolution (Hut 1980; Ogilvie 2014; Damiani & Lanza 2015). Therefore, all our systems are tidally unstable. However, the estimated timescales of tidal evolution are longer than the main-sequence lifetimes of all the systems except for HAT-P-22. Specifically, we can parameterise the efficiency of the dissipation of the tidal kinetic energy inside a star by means of the so-called modified tidal quality factor Q'_s with a faster dissipation and stronger tidal interaction corresponding to a smaller value of Q'_s (e.g. Ogilvie 2014). The value of Q'_s in exoplanet hosts is very uncertain because of our lack of knowledge of the processes that dissipate the energy of the dynamical tides inside main-sequence stars, but the minimum value of Q'_s is generally considered to range between 10^6 and 10^7 (Ogilvie & Lin 2007; Jackson et al. 2009). Adopting such a range of values for HAT-P-3, HAT-P-12, WASP-39, and WASP-60, we find orbital decay timescales between a few times and several tens of times of their main-sequence lifetimes by applying a constant Q'_s version of the tidal evolution model of Leconte et al. (2010). The timescale for the evolution of stellar rotation and orbital obliquity is longer than ~20 Gyr for all these stars. Therefore, their stellar rotation and obliquity have not been significantly affected by tides during their main-sequence evolution. The situation is different in the case of HAT-P-22, which has characteristic timescales of tidal evolution of the rotation and obliquity that range between 0.7 and 7 Gyr for $10^6 \leq Q'_s \leq 10^7$. In this system, tides may have played a role in reducing an initial obliquity of the orbit and accelerating stellar rotation during the main-sequence lifetime of the star.

8. Summary and discussion

As discussed in Sect. 1, it is a difficult task to trace all the steps that occurred during the migration phase of hot Jupiters, and the orbital obliquity could play an important role in disentangling the bundle of possible physical processes. For this purpose a statistical study of a large sample of precise measurements of λ is mandatory. With the present work, we have given another contribution to the enlargement of the sample, by presenting the first measurements of λ for five exoplanetary systems. These systems are HAT-P-3, HAT-P-12, HAT-P-22, WASP-39, and WASP-60, all composed of relatively cold stars, i.e. with $4650\,\mathrm{K} < T_{\mathrm{eff}} < 5490\,\mathrm{K}$, with the exception of WASP-60 for which, based on HARPS-N data, we
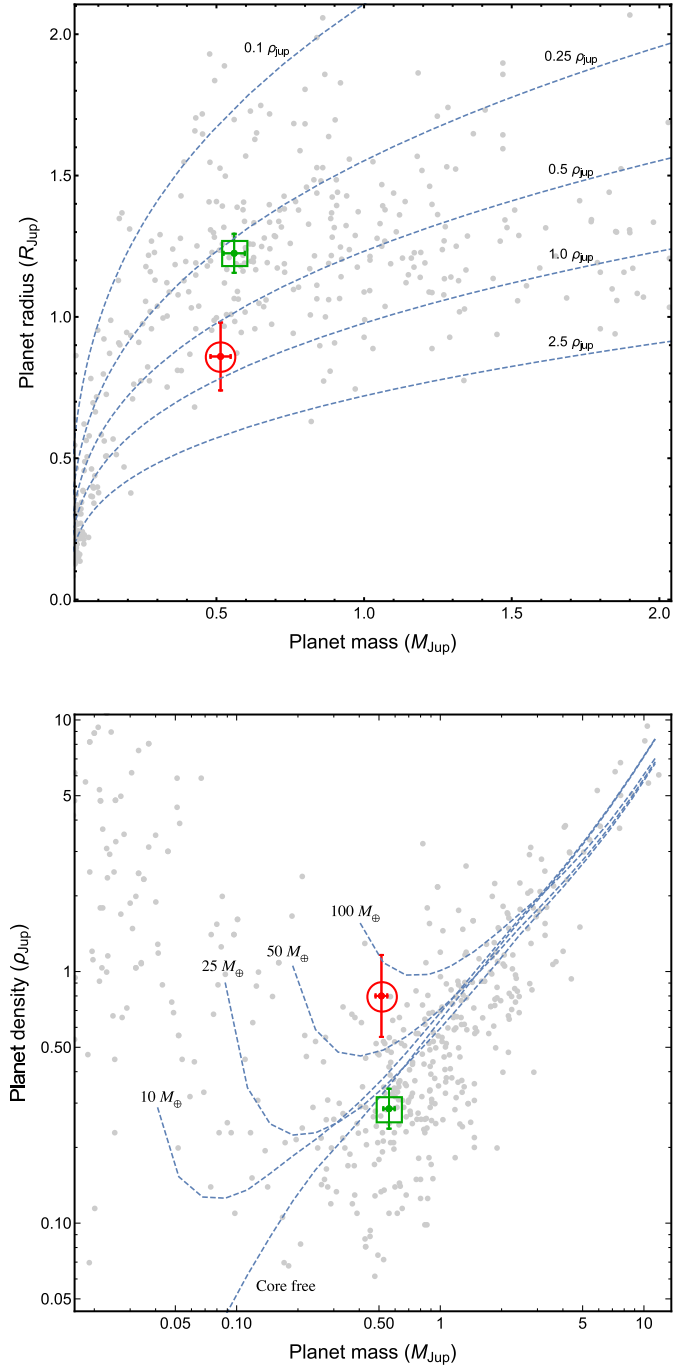
Fig. 9. Mass–radius and mass–density diagrams for known transiting exoplanets. The positions of WASP-60 b are shown in *the both panels* with a green point in a box (this work) and a red point in a circle (Hébrard et al. 2013). The error bars are also illustrated. The grey points denote values taken from TEPCat and their error bars are suppressed for clarity. *Top panel*: a zoom of the mass–radius diagram of known transiting exoplanets. Dashed lines show where density is 2.5, 1.0, 0.5, 0.25, and 0.1 ρ_{Jup}. *Bottom panel*: mass–density diagram of known transiting exoplanets. Dashed lines refer to four planetary models with various core masses and another one without a core (Fortney et al. 2007).

estimated a hotter temperature, i.e. $T_{\mathrm{eff}} = 6105 \pm 50\,\mathrm{K}$. As shown in Sect. 6.3, the spins of two of these systems (HAT-P-22 and WASP-39) are well aligned with the planetary orbital axis. Instead, the orbit of the exoplanet HAT-P-3 b is slightly misaligned, while that of HAT-P-12 b seems strongly misaligned,
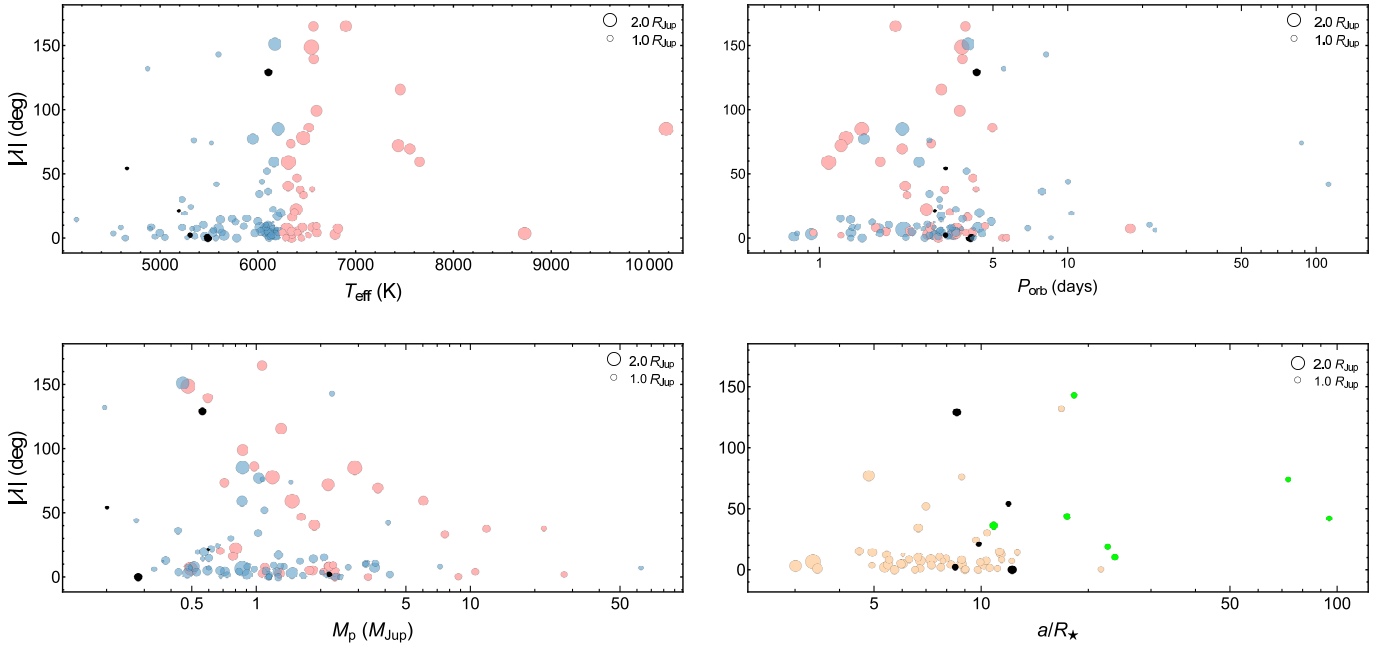
Fig. 10. Sky-projected orbital obliquity as a function of several stellar, orbital, and planetary parameters. We only considered exoplanets with $R_p > 0.8\,R_{Jup}$. The data are taken from TEPCat with the exception of the black points that indicate the five planetary systems examined in this work. *Top left panel*: value λ vs. the effective temperature of the parent stars. Blue (red) circles indicate systems in which the parent star has an effective temperature lower (higher) than 6250 K. The size of each circle is proportional to the corresponding planetary radius. The error bars are suppressed for clarity. *Top right panel*: value λ vs. the orbital period of the planets. The symbols are the same as in *top left panel*. *Bottom left panel*: value λ vs. the planet mass. The symbols are the same as in *top left panel*. *Bottom right panel*: value λ vs. the scaled orbital distance, $a/R_\star$, for those systems with $T_{eff} < 6150\,K$ (Anderson et al. 2015). The black and light orange circles represent planets with near-circular orbits ($e < 0.1$ or consistent with zero; Bonomo et al. 2017), while the green circles depict eccentric orbits ($e \geq 0.1$).

even thought we were not able to put robust constraints on our measurements. Finally, WASP-60 b is in a retrograde orbit.

All these new values are reported in Fig. 10 (black circles), together with the other 107 known transiting exoplanets, for which precise measurements of λ exist[10] and having a radius larger than $0.8\,R_{Jup}$. The last choice was adopted to select a homogeneous sample of giant planets. Basically, we excluded the very few exoplanets in the Neptunian and super-Earth range for which a measurement of the RM effect was performed. The values of λ are plotted as a function of stellar effective temperature (top left panel), planetary orbital period (top right panel), planet mass (bottom left panel), and orbital distance in units of stellar radii, $a/R_\star$ (bottom right panel). Following Esposito et al. (2017) and references therein, in the first three panels, we divided the data into two groups, according to the temperature of the parent stars. These groups are shown with red circles for $T_{eff} \geq 6250\,K$ and blue circles for $T_{eff} < 6250\,K$.

An inspection of the top left panel tells us that the orbit of most of the planets is well aligned for a large range of T_{eff}. The region between 6000 and 6500 K appears very crucial, as many planets present a large misalignment. However the presence of several exceptions at lower and higher temperatures make us think there might be an observational bias, implying the necessity to investigate these two zones of the parameter space, where the measurement of λ is more challenging.

Whereas the top right panel does not provide any particular insight, the bottom left panel confirms something that was already observed by Hébrard et al. (2011), that is the more

massive planets ($M_p > 4\,M_{Jup}$) can be misaligned but are not retrograde.

Finally, in the bottom right panel, we plotted the projected orbital obliquity of the cool-star systems, i.e. following Anderson et al. (2015), those with $T_{eff} < 6150\,K$, as a function of $a/R_\star$. The orange circles represent exoplanets with near-circular orbits ($e < 0.1$) and the green circles eccentric orbits ($e \geq 0.1$). The systems HAT-P-3, HAT-P-12, HAT-P-22, WASP-39, and WASP-60 are again represented with black circles and have e consistent with zero (Bonomo et al. 2017). Anderson et al. (2015) noted that orbits with $a/R_\star < 15$ are circular and the corresponding values of λ are confined within $\sim20°$ of aligned; the distribution of λ is broad at greater separations, where eccentric orbits seem to be preferred. Based on a larger sample, the confinement of λ is not completely convincing. We stress that any inference on the possible trend of higher eccentricity, larger separation companions that are found on typically misaligned orbits, still relies on small-number statistics.

To summarise the results of the photometric time series, in two cases (WASP-60 and HAT-P-12) there is no clear periodicity. In one case (WASP-39) we found a possible periodicity, but it is probably spurious. In another case (HAT-P-3) we detected a periodicity that is promising but below the level of significance. Finally, in the fifth case (HAT-P-22) we were able to propose a more robust detection of the rotational period, i.e. 28.7 ± 0.4 days. Knowing the rotation period of HAT-P-22, we can measure its rotational velocity and, therefore, the inclination of its spin. It is then straightforward to estimate the true misalignment angle of HAT-P-22 b, which is $\psi = 25° \pm 18°$. A more precise determination of the $v \sin i_\star$ is necessary to better constrain this value.

---

[10] Data taken from TEPCat (Southworth 2011).

We finally reviewed the main physical parameters of the five exoplanetary systems. This analysis was performed following the homogeneous studies approach (Southworth 2012), and based on the HARPS-N data and on both 17 new photometric light curves and others taken from the literature. In four cases (see Tables C.1–C.4), we found good agreements with the values reported in the literature. However, for the case of the WASP-60 planetary system, many of the physical characteristics of both the planet and star are very different from those reported by Hébrard et al. (2013); see Table C.5. In particular WASP-60 b is larger and therefore much less dense. We emphasise that, based on our photometric follow-up monitoring of a complete transit of WASP-60 b, we measured a transit depth ≈33% deeper than that presented in the discovery paper, which is only based on survey data and on a single incomplete follow-up light curve (Hébrard et al. 2013). The modelling of incomplete transit light curves can lead to incorrect estimation of the photometric parameters ($R_p/R_\star$, $a/R_\star$, i), contact points and, therefore, stellar density (Mancini & Southworth 2016). The present case of WASP-60 is a good example of this effect.

References

Addison, B. C., Tinney, C. G., Wright, D. J., et al. 2013, ApJ, 774, L9
Albrecht, S., Winn, J. N., Johnson, J. A., et al. 2012, ApJ, 757, 18
Anderson, D. R., Triaud, A. H. M. J., Turner, O. D., et al. 2015, ApJ, 800, L9
Bakos, G. Á., Hartman, J., Torres, G., et al. 2011, ApJ, 742, 116
Baştürk, Ö., Hinse, T. C., Özavc, İ., et al. 2015, ASP Conf. Ser., 496, 370
Baranne, A., Queloz, D., Mayor, M., et al. 1996, A&AS, 119, 373
Batygin, K., Bodenheimer, P. H., & Laughlin, G. P. 2016, ApJ, 829, 114
Biazzo, K., D'Orazi, V., Desidera, S., et al. 2012, MNRAS, 427, 2905
Bitsch, B., & Kley, W. 2011, A&A, 530, A41
Bodenheimer, P., Hubickyj, O., & Lissauer, J. J. 2000, Icarus, 143, 2
Boley, A. C., Granados Contreras, A. P., & Gladman, B. 2016, ApJ, 817, L17
Bonomo, A. S., Desidera, S., Benatti, S., et al. 2017, A&A, 602, A107
Bourrier, V., Cegla, H. M., Lovis, C., & Wyttenbach, A. 2017, A&A, 599, A33
Carter J. A., & Winn J. N., 2009, ApJ, 704, 51

Carpino, M., Milani, A., & Nobili, A. M., 1987, A&A, 181, 182
Chan, T., Ingemyr, M., & Winn, J. N. 2011, AJ, 141, 179
Chatterjee, S., Ford, E. B., Matsumura, S., & Rasio, F. A. 2008, ApJ, 686, 580
Ciceri, S., Mancini, L., Southworth, J., et al. 2015, A&A, 577, A54
Cosentino, R., Lovis, C., Pepe, F., et al. 2012, Proc. SPIE, 8446, 1
Cosentino, R., Lovis, C., Pepe, F., et al. 2014, Proc. SPIE, 9147, 8
Covino, E., Esposito, M., Barbieri, M., et al. 2013, A&A, 554, A28
D'Orazi, V., Biazzo, K., & Randich, S. 2011, A&A, 526, A103
Damiani, C., & Lanza, A. F. 2015, A&A, 574, A39
Dawson, R. I. 2014, ApJ, 790, 31
Eastman, J., Gaudi, B. S., & Agol, E. 2013, PASP, 125, 83
Esposito, M., Covino, E., Mancini, L., et al. 2014, A&A, 564, L13
Esposito, M., Covino, E., Desidera, S., et al. 2017, A&A, 601, A53
Fabrycky, D., & Tremaine, S. 2007, ApJ, 669, 1298
Faedi, F., Barros, S. C. C., & Anderson, D. R. 2011, A&A, 531, A40
Ferraz-Mello, S., Tadeu dos Santos, M., Folonier, H., et al. 2015, ApJ, 807, 78
Fischer, P. D., Knutson, H. A., Sing, D. K., et al. 2016, ApJ, 827, 19
Fortney, J. J., Marley, M. S., & Barnes J. W. 2007, ApJ, 659, 1661
Gibson, N. P., Pollacco, D. L., Barros, S., et al. 2010, MNRAS, 401, 1917
Hartman, J., Bakos, G.Á., Torres, G., et al. 2009, ApJ, 706, 785
Hébrard, G., Ehrenreich, D., Bouchy, F., et al. 2011, A&A, 527, L11
Hébrard, G., Collier Cameron, A., Brown, D. J. A., et al. 2013, A&A, 549, A134
Hinse, T. C., Han, W., Yoon, J.-N., et al. 2015, J. Astron. Space Sci., 32, 21
Hut, P. 1980, A&A, 92, 167
Jackson, B., Barnes, R., & Greenberg, R. 2009, ApJ, 698, 1357
Kammer, J. A., Knutson, H. A., Line, M. R., et al. 2015, ApJ, 810, 118
Kilpatrick, B. M., Lewis, N. K., Kataria, T., et al. 2017, AJ, 153, 22
Knutson, H. A., Fulton, B., J., Montet, B. T., et al. 2014, ApJ, 785, 126
Kuschnig, R., Weiss, W. W., Gruber, R., Bely, P. Y., & Jenkner, H. 1997, A&A, 328, 544
Leconte, J., Chabrier, G., Baraffe, I., & Levrard, B. 2010, A&A, 516, A64
Lee, J. W., Youn, J.-H., Kim, S.-L., et al. 2012, AJ, 143, 95
Lin, D. N. C., Bodenheimer, P., Richardson, D. C. 1996, Nature, 380, 606
Line, M. R., Knutson, H., Deming, D., et al. 2013, ApJ, 778, 183
Lovis, C., & Pepe, F. 2007, A&A, 468, 1115
Lovis, C., Dumusque, X., Santos, N. C., et al. 2011, ArXiv e-prints [arXiv:1107.5325]
Maciejewski, G., Dimitrov, D., Mancini, L., et al. 2016, Acta Astron., 66, 55
Madhusudhan, N., & Winn, J. N. 2009, ApJ, 693, 784
Mallonn, M., Nascimbeni, V., Weingrill, J., et al. 2015, A&A, 583, A138
Mamajek, E. E., & Hillenbrand, L. A. 2008, ApJ, 687, 1264
Mancini L., & Southworth J., 2016, in Twenty Years of Giant Exoplanets, Proc. Haute Provence Observatory Colloquium, eds. I. Boisse, O. Demangeon, F. Bouchy, & L. Arnold (Observ. de Haute-Provence, Institut Pytheas) 120
Mancini, L., Southworth, J., Ciceri, S., et al. 2013, A&A, 551, A11
Mancini, L., Southworth, J., Ciceri, S., et al. 2014, MNRAS, 443, 2391
Mancini, L., Esposito, M., Covino, E., et al. 2015, A&A, 579, A136
Mancini, L., Southworth, J., Raia, G., et al. 2017, MNRAS, 465, 843
Marzari, F. 2014, MNRAS, 444, 1419
Marzari, F., & Nelson, Andrew F. 2009, ApJ, 705, 1575
McQuillan, A., Mazeh, T., & Aigrain, S. 2014, ApJS, 211, 24
Nagasawa, M., Ida, S., Bessho, T. 2008, ApJ, 678, 498
Naoz, S., Farr, W. M., Lithwick, Y., et al. 2011, Nature, 473, 187
Nascimbeni, V., Piotto, G., Bedin, L. R., & Damasso, M. 2011, A&A, 527, A85
Nelson, B. E., Ford, E. B., Rasio, F. A., et al. 2017, AJ, 154, 106
Nikolov, N., Sing, D. K., Gibson, N. P., et al. 2016, ApJ, 832, 191
Noyes, R. W., Hartmann, L. W., Baliunas, S. L. et al. 1984, ApJ, 279, 763
Ogilvie, G. I. 2014, ARA&A, 52, 171
Ogilvie, G. I., & Lin, D. N. C. 2007, ApJ, 661, 1180
Pepe, F., Mayor, M., Galland, F., et al. 2002, A&A, 388, 632
Pont, F., Husnoo, N., Mazeh, T., & Collier Cameron, D. 2011, MNRAS, 414, 1278
Queloz, D., Anderson, D. R., & Collier Cameron, A., et al. 2010, A&A, 517, L1
Rasio, F. A., & Ford, E. B. 1996, Science, 274, 954
Ricci, D., Ramón-Fox, F., G., Ayala-Loera, C., et al. 2015, PASP, 127, 143
Ricci, D., Sada, P. V., Navarro-Meza, S., et al. 2017, PASP, 129, 064401
Sada, P. V., & Ramón-Fox, F. G. 2016, PASP, 128, 024402
Sada, P. V., Deming, D., & Jennings, D. E. 2012, PASP, 124, 212
Schlaufman, K. C. 2010, ApJ, 719, 602
Smareglia, R., Bignamini, A., Knapic, C., Molinaro, M., & GAPS Collaboration 2014, in Astronomical Data Analysis Software and Systems XXIII, eds. N. Manset, & P. Forshay, ASP Conf. Ser., 485, 435
Sneden, C. 1973, ApJ, 184, 839
Sousa, S. G., Santos, N. C., Israelian, G., et al. 2007, A&A, 469, 783
Sousa, S. G., Alapini, A., Israelian, G., & Santos, N. C. 2010, A&A, 512, A13
Sousa, S. G., Santos, N. C., Mortier, A., et al. 2015, A&A, 576, A94
Southworth, J. 2009, MNRAS, 394, 272
Southworth, J. 2011, MNRAS, 417, 2166

Southworth, J. 2012, MNRAS, 426, 1291
Southworth J., 2013, A&A, 557, A119
Southworth, J., Hinse, T. C., Jørgensen, U. G., et al. 2009, MNRAS, 396, 1023
Southworth, J., Mancini, L., Maxted, P. F. L., et al. 2012, MNRAS, 422, 3099
Southworth, J., Hinse, T. C., Burgdorf, M., et al. 2014, MNRAS, 444, 776
Todorov, K. O., Deming, D., Knutson, H. A., et al., 2013, ApJ, 770, 102
Torres, G., Bakos, G.Á., Kovács, G., et al. 2007, ApJ, 666, L121
Torres, G., Winn, J. N., & Holman, M. J. 2008, ApJ, 677, 1324

Torres, G., Fischer, D. A., Sozzetti, A., et al. 2012, ApJ, 757, 161
Turner, J. D., Pearson, K. A., Biddle, L. I., et al. 2016, MNRAS, 459, 789
Turner, J. D., Leiter, R. M., Biddle, L. I., et al. 2017, MNRAS, 472, 3871
Valsecchi, F., & Rasio, F. A. 2014, ApJ, 786, 102
Vaniĉek, P. 1971, Ap&SS, 12, 10
Winn, J. N., Holman, M. J., Henry, G. W., et al. 2007, AJ, 133, 1828
Winn, J. N., Fabrycky, D., Albrecht, S., & Johnson, J. A. 2010, ApJ, 718, L145
Zhou, G., Bayliss, D., Hartman, J. D., et al. 2015, ApJ, 814, L16

Appendix A: Details of the spectroscopic and photometric observations

The tables in this appendix report the details of the spectroscopic and photometric observations that were presented in this work. In particular, Table A.1 shows the log of the HARPS-N observations, while Table A.2 the log concerning all the photometric follow-up observations.

Table A.1. Details of the spectroscopic HARPS-N observations presented in this work.

Object	Type	Date[a]	UT Start	UT End	N_{obs}	T_{exp}[s]	Airmass[b]	Moon[c]	2nd fibre
HAT-P-3	K5	2013.06.10	20:58	01:03	22	600	$1.07 \rightarrow 1.06 \rightarrow 1.38$	NO	ThAr lamp
WASP-60	F9[d]	2013.10.20	21:08	02:59	21	900	$1.07 \rightarrow 1.00 \rightarrow 1.59$	95%/49°	Sky
HAT-P-22	G2	2014.04.03	22:25	03:47	31	600	$1.06 \rightarrow 1.07 \rightarrow 1.96$	NO	ThAr lamp
HAT-P-12	K5	2015.03.13	00:59	06:22	21(17)	900	$1.20 \rightarrow 1.03 \rightarrow 1.22$	46%/81°	Sky
		2015.04.24	20:56	01:02	16	900	$1.48 \rightarrow 1.03$	41%/82°	Sky
WASP-39	K5	2015.05.04	22:54	04:02	20	900	$1.32 \rightarrow 1.18 \rightarrow 1.79$	99%/19°[e]	Sky

Notes. [a]Dates refer to the beginning of the night. [b]Values at first → last exposure, or first → meridian → last exposure. [c]Fraction of illumination and angular distance from the target. [d]This work. [e]We checked that the nearby full Moon (RV = $-3.5 \, \mathrm{km \, s^{-1}}$) did not contaminate the CCF profiles and had no effect on the RV measurements (see Esposito et al. 2017).

Table A.2. Details of the photometric follow-up observations presented in this work.

Telescope	Date of first obs	Start time (UT)	End time (UT)	N_{obs}	T_{exp} (s)	Filter	Airmass	Moon illum.	Aperture radii (px)	Scatter (mmag)
HAT-P-3										
Cassini	2010.06.07	20:12	00:16	107	60–150	Gunn *i*	$1.01 \rightarrow 1.35$	22%	16, 26, 50	1.69
CA 1.23 m	2015.05.01	20:09	03:52	246	85	Cousins *I*	$1.22 \rightarrow 1.03 \rightarrow 1.50$	96%	17, 40, 60	1.49
CA 1.23 m	2015.05.07	19:45	02:23	178	102–135	Cousins *I*	$1.21 \rightarrow 1.03 \rightarrow 1.28$	84%	22, 45, 70	0.66
CA 1.23 m	2015.06.02	20:28	03:01	183	98–130	Cousins *I*	$1.04 \rightarrow 1.03 \rightarrow 2.20$	100%	20, 45, 70	0.83
HAT-P-12										
INT	2010.04.29	02:28	05:47	91	100	Gunn *r*	$1.12 \rightarrow 2.15$	97%	20, 40, 60	0.92
CA 2.2 m	2010.05.11	21:11	03:54	151	80–120	Strömgren *u*	$1.07 \rightarrow 1.03 \rightarrow 1.74$	5%	9, 14, 30	5.97
CA 2.2 m	2010.05.11	21:11	03:54	157	80–120	Gunn *g*	$1.07 \rightarrow 1.03 \rightarrow 1.74$	5%	25, 35, 60	1.14
CA 2.2 m	2010.05.11	21:11	03:54	146	80–120	Gunn *r*	$1.07 \rightarrow 1.03 \rightarrow 1.74$	5%	28, 38, 70	1.04
CA 2.2 m	2010.05.11	21:11	03:54	166	80–120	Johnson *I*	$1.07 \rightarrow 1.03 \rightarrow 1.74$	5%	25, 35, 60	1.32
CA 1.23 m	2012.03.06	23:41	05:33	83	105–130	Cousins *R*	$1.31 \rightarrow 1.00 \rightarrow 1.13$	97%	24, 45, 70	1.38
Cassini	2012.04.21	01:38	03:24	47	120	Gunn *r*	$1.20 \rightarrow 1.61$	0%	20, 55, 85	1.27
CA 1.23 m	2013.06.15	20:48	01:44	146	70–120	Cousins *R*	$1.00 \rightarrow 2.05$	41%	23, 48, 70	1.22
CA 1.23 m	2014.03.16	00:55	05:23	152	85–100	Cousins *I*	$1.07 \rightarrow 1.00 \rightarrow 1.17$	100%	28, 50, 72	1.06
CA 1.23 m	2014.04.13	20:58	03:42	156	120–150	Cousins *I*	$1.44 \rightarrow 1.00 \rightarrow 1.21$	98%	35, 55, 75	0.94
CA 1.23 m	2015.06.24	21:58	01:35	95	120	Cousins *R*	$1.07 \rightarrow 2.13$	55%	26, 54, 80	1.49
CA 1.23 m	2016.07.04	20:33	01:29	164	95	Cousins *R*	$1.04 \rightarrow 2.66$	1%	18, 35, 50	1.62
WASP-60										
CA 12.3 m	2014.10.21	18:40	01:57	233	100	Cousins *I*	$1.70 \rightarrow 1.00 \rightarrow 1.28$	3%	19, 27, 50	0.68

Notes. N_{obs} is the number of observations, T_{exp} is the exposure time, and "Moon illum." is the geocentric fractional illumination of the Moon at midnight (UT). The aperture sizes are the radii of the software apertures for the star, inner sky, and outer sky, respectively. Scatter is the *rms* scatter of the data vs. a fitted model.

Appendix B: HARPS-N RV measurements

The RV measurements, which were obtained with HARPS-N (this work), are reported in this appendix.

Table B.1. HARPS-N RV measurements of HAT-P-3.

BJD (TDB)	RV (m s^{-1})	Error (m s^{-1})	S/N
2 456 454.378444	−23367.2	2.0	39.1
2 456 454.385689	−23371.8	2.1	38.9
2 456 454.392929	−23372.4	2.1	39.6
2 456 454.400166	−23373.7	1.9	41.6
2 456 454.407406	−23373.5	1.9	42.2
2 456 454.414647	−23377.3	1.9	42.0
2 456 454.421896	−23375.2	1.9	41.8
2 456 454.429142	−23374.5	1.0	40.7
2 456 454.436382	−23378.5	2.2	38.2
2 456 454.443623	−23380.5	2.6	33.5
2 456 454.450868	−23384.2	4.2	23.0
2 456 454.458118	−23389.8	3.1	28.8
2 456 454.465363	−23393.0	2.7	32.5
2 456 454.481173	−23398.0	2.7	32.3
2 456 454.488422	−23403.4	3.6	25.9
2 456 454.495667	−23395.2	3.9	24.7
2 456 454.502908	−23394.1	5.0	20.5
2 456 454.512501	−23402.5	4.5	22.2
2 456 454.519746	−23400.1	7.0	15.8
2 456 454.526986	−23400.9	5.3	19.6
2 456 454.534227	−23399.6	6.1	17.5
2 456 454.541477	−23397.2	4.5	22.3

Table B.2. HARPS-N RV measurements of HAT-P-12.

BJD (TDB)	RV (m s^{-1})	Error (m s^{-1})	S/N
2 457 095.593419	−40450.2	6.0	17.0
2 457 095.604117	−40452.4	6.6	15.9
2 457 095.614820	−40456.4	7.6	14.6
2 457 095.625522	−40455.5	11.1	10.8
2 457 095.636220	−40451.7	6.9	15.6
2 457 095.646928	−40448.7	5.9	17.4
2 457 095.657626	−40459.3	6.1	17.1
2 457 095.668328	−40456.7	7.9	14.3
2 457 095.679040	−40464.1	6.8	15.7
2 457 095.689748	−40466.1	7.3	15.0
2 457 095.700450	−40463.9	5.6	18.1
2 457 095.711153	−40465.3	8.4	13.3
2 457 095.721860	−40454.8	10.5	11.4
2 457 095.732559	−40467.9	11.9	10.3
2 457 095.743267	−40471.2	8.6	13.4
2 457 095.753974	−40466.5	8.3	13.9
2 457 095.764682	−40466.7	6.7	16.3
2 457 137.381494	−40462.4	10.2	12.3
2 457 137.392206	−40453.1	9.5	13.0
2 457 137.402913	−40462.6	8.6	14.0
2 457 137.413619	−40436.0	8.6	14.2
2 457 137.424331	−40440.6	7.8	15.2
2 457 137.435038	−40448.0	7.0	16.2
2 457 137.445740	−40454.1	7.0	16.0
2 457 137.456452	−40461.4	9.6	13.1
2 457 137.467149	−40457.3	8.6	14.1
2 457 137.477861	−40476.8	8.5	14.1
2 457 137.488563	−40457.1	7.3	15.5
2 457 137.499261	−40466.6	8.4	14.4
2 457 137.509963	−40460.5	7.8	15.1
2 457 137.520678	−40469.5	6.2	17.4
2 457 137.531385	−40463.8	5.2	19.9
2 457 137.542087	−40467.9	5.6	18.7

Table B.3. HARPS-N RV measurements of HAT-P-22.

BJD (TDB)	RV (m s^{-1})	Error (m s^{-1})	S/N
2 456 751.440813	12706.6	1.0	75.6
2 456 751.448034	12704.0	1.0	74.1
2 456 751.455255	12698.5	0.9	78.5
2 456 751.462476	12695.3	0.9	77.7
2 456 751.469698	12692.3	0.9	79.1
2 456 751.476918	12686.9	0.9	79.0
2 456 751.484144	12682.6	0.9	76.5
2 456 751.491369	12679.0	0.9	76.5
2 456 751.498599	12674.0	0.9	77.4
2 456 751.505829	12673.3	1.0	75.1
2 456 751.513055	12674.7	1.2	64.4
2 456 751.520281	12671.4	1.4	54.4
2 456 751.527507	12663.7	1.4	56.1
2 456 751.534733	12661.5	1.5	53.2
2 456 751.541962	12649.6	1.5	52.9
2 456 751.549192	12645.5	1.6	49.3
2 456 751.556422	12638.4	1.5	50.8
2 456 751.563635	12630.0	1.4	54.1
2 456 751.570857	12624.3	1.4	55.1
2 456 751.578086	12616.2	1.7	47.5
2 456 751.585320	12606.8	2.2	38.5
2 456 751.592554	12604.2	1.8	44.1
2 456 751.599775	12595.6	1.7	47.4
2 456 751.606998	12602.5	1.6	48.7
2 456 751.614219	12600.7	1.4	57.0
2 456 751.621450	12595.8	1.4	54.2
2 456 751.628670	12591.0	1.4	56.9
2 456 751.635900	12586.9	1.3	59.6
2 456 751.643130	12583.6	1.4	57.1
2 456 751.650352	12579.3	1.4	57.6
2 456 751.657573	12573.8	1.5	53.7

Table B.5. HARPS-N RV measurements of WASP-60.

BJD (TDB)	RV (m s^{-1})	Error (m s^{-1})	S/N
2 456 586.391049	−26529.3	6.0	25.4
2 456 586.409541	−26520.0	5.6	27.0
2 456 586.420258	−26530.0	5.3	27.8
2 456 586.430971	−26527.3	5.8	26.1
2 456 586.441693	−26516.7	6.2	24.5
2 456 586.452402	−26533.3	6.1	24.9
2 456 586.463115	−26524.3	5.9	25.1
2 456 586.473828	−26521.7	6.5	23.5
2 456 586.494129	−26516.8	5.4	28.0
2 456 586.504856	−26525.2	6.2	25.3
2 456 586.515582	−26515.0	5.0	29.4
2 456 586.526300	−26512.1	5.2	28.7
2 456 586.537013	−26524.9	6.4	24.6
2 456 586.547726	−26516.0	6.9	23.5
2 456 586.558439	−26517.0	5.5	27.9
2 456 586.569156	−26533.6	5.7	27.3
2 456 586.579878	−26536.4	5.5	28.4
2 456 586.590596	−26532.6	6.3	25.8
2 456 586.601309	−26541.0	6.1	26.6
2 456 586.612026	−26544.7	6.1	26.5
2 456 586.624506	−26539.0	5.7	28.1

Table B.4. HARPS-N RV measurements of WASP-39.

BJD (TDB)	RV (m s^{-1})	Error (m s^{-1})	S/N
2 457 147.465780	−58445.5	9.7	14.2
2 457 147.476477	−58438.3	9.6	14.1
2 457 147.487180	−58439.0	6.2	19.7
2 457 147.497878	−58431.0	5.7	21.2
2 457 147.508575	−58444.0	7.5	17.3
2 457 147.519282	−58436.0	4.9	23.8
2 457 147.529990	−58417.3	4.7	24.4
2 457 147.540692	−58434.3	5.1	22.8
2 457 147.551390	−58435.3	5.2	22.6
2 457 147.562097	−58436.9	5.0	23.2
2 457 147.572794	−58437.5	5.0	23.5
2 457 147.583501	−58448.9	5.0	23.4
2 457 147.594208	−58453.1	4.5	25.0
2 457 147.604906	−58466.1	4.7	24.4
2 457 147.615604	−58459.3	4.5	25.3
2 457 147.626324	−58448.4	4.8	24.3
2 457 147.637027	−58446.9	4.7	24.6
2 457 147.647729	−58432.9	5.3	23.1
2 457 147.658427	−58452.3	4.6	25.3
2 457 147.669133	−58445.1	5.9	20.9

Appendix C: Revised physical parameters of the five planetary systems

The tables in this appendix report the values of the main physical parameters of the five planetary systems under study. The values obtained in this work (Sect. 7) are compared with those taken from the literature. Where two error bars are given, the first refers to the statistical uncertainties and the second to the systematic errors.

Table C.1. Physical parameters of the planetary system HAT-P-3 derived in this work.

Parameter	Nomen.	Unit	This Work	Torres et al. (2008)	Southworth (2012)
Stellar parameters					
Effective temperature	$T_{\rm eff}$	K	5190 ± 80	5185 ± 80	–
Iron abundance	[Fe/H]		$+0.24 \pm 0.08$	$+0.27 \pm 0.00$	–
Projected rotational velocity	$v \sin i_\star$	km s^{-1}	1.4 ± 0.5	0.5 ± 0.5	–
Mass	$M_\star$	$M_\odot$	$0.925 \pm 0.031 \pm 0.034$	$0.928^{+0.044}_{-0.054}$	$0.900 \pm 0.036 \pm 0.044$
Radius	$R_\star$	$R_\odot$	$0.850 \pm 0.021 \pm 0.010$	$0.833^{+0.034}_{-0.044}$	$0.870 \pm 0.016 \pm 0.014$
Mean density	$\rho_\star$	$\rho_\odot$	1.51 ± 0.11	$1.90^{+0.38}_{-0.42}$	1.365 ± 0.078
Logarithmic surface gravity	$\log g_\star$	cgs	$4.545 \pm 0.022 \pm 0.005$	4.564 ± 0.032	$4.513 \pm 0.020 \pm 0.007$
Age		Gyr	$2.9^{+1.7+2.1}_{-3.7-3.2}$	$1.5^{+5.4}_{-1.4}$	$7.5^{+4.2+3.6}_{-3.8-2.7}$
Planetary parameters					
Mass	$M_{\rm p}$	$M_{\rm Jup}$	$0.595 \pm 0.019 \pm 0.015$	$0.596^{+0.024}_{-0.026}$	$0.584 \pm 0.020 \pm 0.019$
Radius	$R_{\rm p}$	$R_{\rm Jup}$	$0.911 \pm 0.032 \pm 0.011$	$0.899^{+0.043}_{-0.049}$	$0.947 \pm 0.027 \pm 0.015$
Mean density	$\rho_{\rm p}$	$\rho_{\rm Jup}$	$0.735 \pm 0.075 \pm 0.009$	$0.77^{+0.14}_{-011}$	$0.643 \pm 0.052 \pm 0.011$
Surface gravity	$g_{\rm p}$	m s^{-2}	17.8 ± 1.2	$20.4^{+3.0}_{-3.1}$	16.14 ± 0.90
Equilibrium temperature	$T_{\rm eq}$	K	1170 ± 17	1127^{+49}_{-39}	1189 ± 16
Safronov number	Θ		$0.0547 \pm 0.0022 \pm 0.0007$	$0.0585^{+0.0044}_{-0.0048}$	$0.0526 \pm 0.0019 \pm 0.0009$
Orbital parameters					
Time of mid-transit	T_0	BJD (TDB)	$2\,457\,150.39472\,(58)$	$2\,454\,218.7594\,(29)$	–
Period	$P_{\rm orb}$	day	$2.89973838\,(27)$	$2.899703\,(54)$	$2.8997360\,(20)$
Semi-major axis	a	au	$0.03878 \pm 0.00044 \pm 0.00048$	$0.03882^{+0.00060}_{-0.00077}$	$0.03842 \pm 0.00050 \pm 0.00063$
Inclination	i	°	86.31 ± 0.19	87.24 ± 0.69	86.15 ± 0.19
RV-curve semi-amplitude	$K_{\rm A}$	m s^{-1}	90.63 ± 0.58^a	89.1 ± 2.0	–
Barycentric RV	γ	km s^{-1}	-23.3849 ± 0.0007	-14.8 ± 0.10	–
Projected spin–orbit angle	λ	°	21.2 ± 8.7	–	–

Notes. [a]This value of $K_{\rm A}$ was determined from out-of-transit RV HIRES+HARPS-N data.

Table C.2. Physical parameters of the planetary system HAT-P-12 derived in this work.

Parameter	Nomen.	Unit	This Work	Hartman et al. (2009)	Lee et al. (2012)
Stellar parameters					
Effective temperature	$T_{\rm eff}$	K	4665 ± 45	4650 ± 60	–
Iron abundance	[Fe/H]		-0.20 ± 0.09	-0.29 ± 0.05	–
Projected rotational velocity	$v \sin i_\star$	km s^{-1}	0.5 ± 0.5	0.5 ± 0.4	–
Mass	$M_\star$	$M_\odot$	$0.691 \pm 0.032 \pm 0.015$	0.733 ± 0.018	0.727 ± 0.019
Radius	$R_\star$	$R_\odot$	$0.679 \pm 0.012 \pm 0.005$	$0.701^{+0.017}_{-0.012}$	0.702 ± 0.013
Mean density	$\rho_\star$	$\rho_\odot$	2.205 ± 0.077	–	2.100 ± 0.089
Logarithmic surface gravity	$\log g_\star$	cgs	$4.614 \pm 0.012 \pm 0.003$	4.75 ± 0.10	4.607 ± 0.020
Age		Gyr	$7.2^{+3.7+5.3}_{-4.4-2.8}$	2.5 ± 2.0	3.2 ± 3.8
Planetary parameters					
Mass	$M_{\rm p}$	$M_{\rm Jup}$	$0.201 \pm 0.011 \pm 0.003$	0.211 ± 0.012	0.210 ± 0.012
Radius	$R_{\rm p}$	$R_{\rm Jup}$	$0.919 \pm 0.022 \pm 0.007$	$0.959^{+0.029}_{-0.021}$	0.936 ± 0.012
Mean density	$\rho_{\rm p}$	$\rho_{\rm Jup}$	$0.242 \pm 0.017 \pm 0.002$	0.222 ± 0.019	0.240 ± 0.012
Surface gravity	$g_{\rm p}$	m s^{-2}	5.89 ± 0.34	5.6 ± 0.4	6.37 ± 0.30
Equilibrium temperature	$T_{\rm eq}$	K	955 ± 11	963 ± 16	960 ± 14
Safronov number	Θ		$0.0238 \pm 0.0012 \pm 0.0002$	0.023 ± 0.001	0.0236 ± 0.0015
Orbital parameters					
Time of mid-transit	T_0	BJD (TDB)	$2\,455\,328.49068\,(19)$	$2\,454\,419.19556\,(20)$	$2\,454\,187.85560\,(11)$
Period	$P_{\rm orb}$	day	$3.21305992\,(35)$	$3.2130598\,(21)$	$3.21305961\,(35)$
Semi-major axis	a	au	$0.03767 \pm 0.00057 \pm 0.00027$	0.0384 ± 0.0003	0.03829 ± 0.00046
Inclination	i	°	89.10 ± 0.24	89.0 ± 0.4	89.915 ± 0.098
RV-curve semi-amplitude	$K_{\rm A}$	m s^{-1}	–	35.8 ± 1.9	–
Barycentric RV	γ	km s^{-1}	-40.4589 ± 0.0023	-40.51 ± 0.21	–
Projected spin–orbit angle	λ	°	-54^{+41}_{-13}	–	–

Table C.3. Physical parameters of the planetary system HAT-P-22 derived in this work.

Parameter	Nomen.	Unit	This Work	Bakos et al. (2011)	Turner et al. (2016)
Stellar parameters					
Effective temperature	$T_{\rm eff}$	K	5314 ± 50	5302 ± 80	–
Iron abundance	[Fe/H]		$+0.30 \pm 0.09$	$+0.24 \pm 0.08$	–
Projected rotational velocity	$v \sin i_\star$	km s^{-1}	1.3 ± 0.7	0.5 ± 0.5	–
Mass	$M_\star$	$M_\odot$	$0.936 \pm 0.028 \pm 0.033$	0.916 ± 0.035	–
Radius	$R_\star$	$R_\odot$	$1.062 \pm 0.046 \pm 0.013$	1.040 ± 0.044	–
Mean density	$\rho_\star$	$\rho_\odot$	0.781 ± 0.099	–	–
Logarithmic surface gravity	$\log g_\star$	cgs	$4.357 \pm 0.039 \pm 0.005$	4.36 ± 0.04	–
Age		Gyr	$9.0^{+1.4 +3.7}_{-2.2 -3.0}$	12.4 ± 2.6	
Planetary parameters					
Mass	$M_{\rm p}$	$M_{\rm Jup}$	$2.192 \pm 0.057 \pm 0.052$	2.147 ± 0.061	2.148 ± 0.062
Radius	$R_{\rm p}$	$R_{\rm Jup}$	$1.060 \pm 0.073 \pm 0.013$	1.080 ± 0.058	1.092 ± 0.047
Mean density	$\rho_{\rm p}$	$\rho_{\rm Jup}$	$1.72 \pm 0.35 \pm 0.02$	$1.59^{+0.3}_{-0.22}$	1.61 ± 0.21
Surface gravity	$g_{\rm p}$	m s^{-2}	48.3 ± 6.6	45.7 ± 5.3	49^{+8}_{-7}
Equilibrium temperature	$T_{\rm eq}$	K	1293 ± 29	1283 ± 32	–
Safronov number	Θ		$0.184 \pm 0.013 \pm 0.002$	0.179 ± 0.010	–
Orbital parameters					
Time of mid-transit	T_0	BJD (TDB)	$2\,454\,930.22016\,(16)$	$2\,454\,931.809\,(16)$	$2\,454\,930.22296\,(25)$
Period	$P_{\rm orb}$	day	$3.21223328\,(58)$	$3.212220\,(9)$	$3.2122312\,(12)$
Semi-major axis	a	au	$0.04171 \pm 0.00042 \pm 0.00050$	0.0414 ± 0.0005	–
Inclination	i	$^\circ$	86.46 ± 0.41	$86.9^{+0.6}_{-0.5}$	–
RV-curve semi-amplitude	$K_{\rm A}$	m s^{-1}	–	313.3 ± 4.2	–
Barycentric RV	γ	km s^{-1}	$+12.63696 \pm 0.00035$	$+12.49 \pm 0.28$	–
Projected spin–orbit angle	λ	$^\circ$	-2.1 ± 3.0	–	–
True spin–orbit angle	ψ	$^\circ$	$1.5^{\circ}\,{}^{+30.0^\circ}_{-1.5^\circ}$	–	–

Table C.4. Physical parameters of the planetary system WASP-39 derived in this work.

Parameter	Nomen.	Unit	This Work	Faedi et al. (2011)	Maciejewski et al. (2016)
Stellar parameters					
Effective temperature	$T_{\rm eff}$	K	5485 ± 50	5400 ± 150	–
Iron abundance	[Fe/H]		$+0.01 \pm 0.09$	-0.12 ± 0.10	–
Projected rotational velocity	$v \sin i_\star$	km s^{-1}	1.0 ± 0.5	1.4 ± 0.6	–
Mass	$M_\star$	$M_\odot$	$0.913 \pm 0.035 \pm 0.031$	0.93 ± 0.03	–
Radius	$R_\star$	$R_\odot$	$0.939 \pm 0.019 \pm 0.011$	0.895 ± 0.023	$0.918^{+0.022}_{-0.019}$
Mean density	$\rho_\star$	$\rho_\odot$	1.103 ± 0.057	$1.297^{+0.082}_{-0.074}$	$1.201^{+0.075}_{-0.063}$
Logarithmic surface gravity	$\log g_\star$	cgs	$4.453 \pm 0.017 \pm 0.005$	4.503 ± 0.017	$4.480^{+0.029}_{-0.025}$
Age		Gyr	$8.5^{+3.5 +2.0}_{-1.0 -3.3}$	9^{+3}_{-4}	–
Planetary parameters					
Mass	$M_{\rm p}$	$M_{\rm Jup}$	$0.281 \pm 0.031 \pm 0.006$	0.28 ± 0.03	0.283 ± 0.041
Radius	$R_{\rm p}$	$R_{\rm Jup}$	$1.279 \pm 0.037 \pm 0.014$	1.27 ± 0.04	$1.332^{+0.034}_{-0.031}$
Mean density	$\rho_{\rm p}$	$\rho_{\rm Jup}$	$0.126 \pm 0.017 \pm 0.001$	0.14 ± 0.02	$0.120^{+0.020}_{-0.019}$
Surface gravity	$g_{\rm p}$	m s^{-2}	4.26 ± 0.50	4.07 ± 0.46	$4.14^{+0.62}_{-0.61}$
Equilibrium temperature	$T_{\rm eq}$	K	1166 ± 14	1116^{+33}_{-32}	–
Safronov number	Θ		$0.0232 \pm 0.0025 \pm 0.0003$	–	–
Orbital parameters					
Time of mid-transit	T_0	BJD (TDB)	$2\,455\,342.96913\,(63)$	$2\,455\,342.9688\,(2)$	$2\,455\,342.96982\,(51)$
Period	$P_{\rm orb}$	day	$4.0552941\,(34)$	$4.055259\,(9)$	$4.0552765\,(35)$
Semi-major axis	a	au	$0.04828 \pm 0.00061 \pm 0.00054$	0.0486 ± 0.0005	0.04858 ± 0.00052
Inclination	i	$^\circ$	87.32 ± 0.17	$87.83^{+0.25}_{-0.22}$	$87.75^{+0.27}_{-0.20}$
RV-curve semi-amplitude	$K_{\rm A}$	m s^{-1}	–	38 ± 4	37.9 ± 5.4
Barycentric RV	γ	km s^{-1}	-58.4421 ± 0.0020	-58.4826 ± 0.0004	–
Projected spin–orbit angle	λ	$^\circ$	0 ± 11	–	–

Table C.5. Physical parameters of the planetary system WASP-60 derived in this work.

Parameter	Nomen.	Unit	This Work	Hébrard et al. (2013)	Turner et al. (2017)
Stellar parameters					
Effective temperature	$T_{\rm eff}$	K	6105 ± 50	5900 ± 100	–
Iron abundance	[Fe/H]		$+0.26 \pm 0.07$	-0.04 ± 0.09	–
Projected rotational velocity	$v \sin i_\star$	km s^{-1}	3.8 ± 0.6	3.4 ± 0.8	–
Mass	$M_\star$	$M_\odot$	$1.229 \pm 0.026 \pm 0.015$	1.078 ± 0.035	–
Radius	$R_\star$	$R_\odot$	$1.401 \pm 0.066 \pm 0.006$	1.14 ± 0.13	–
Mean density	$\rho_\star$	$\rho_\odot$	0.447 ± 0.063	0.72 ± 0.20	–
Logarithmic surface gravity	$\log g_\star$	cgs	$4.235 \pm 0.041 \pm 0.002$	4.35 ± 0.09	–
Age		Gyr	$1.7^{+0.5\,+0.4}_{-0.5\,-0.2}$	9^{+3}_{-4}	–
Planetary parameters					
Mass	$M_{\rm p}$	$M_{\rm Jup}$	$0.560 \pm 0.036 \pm 0.005$	0.514 ± 0.034	0.512 ± 0.034
Radius	$R_{\rm p}$	$R_{\rm Jup}$	$1.225 \pm 0.069 \pm 0.005$	0.86 ± 0.12	0.94 ± 0.12
Mean density	$\rho_{\rm p}$	$\rho_{\rm Jup}$	$0.285 \pm 0.052 \pm 0.001$	0.8 ± 0.3	0.75 ± 0.27
Surface gravity	$g_{\rm p}$	m s^{-2}	9.2 ± 1.2	$15.5^{+4.9}_{-3.7}$	12.8 ± 6.5
Equilibrium temperature	$T_{\rm eq}$	K	1479 ± 35	1320 ± 75	1354 ± 23
Safronov number	Θ		$0.0411 \pm 0.0036 \pm 0.0002$	–	0.051 ± 0.013
Orbital parameters					
Time of mid-transit	T_0	BJD (TDB)	$2\,456\,952.43264\,(17)$	$2\,455\,747.0295\,(22)$	$2\,455\,747.0302\,(22)$
Period	$P_{\rm orb}$	day	$4.3050040\,(59)$	$4.3050011\,(62)$	$4.305022\,(21)$
Semi-major axis	a	au	$0.05548 \pm 0.00040 \pm 0.00023$	0.0531 ± 0.0006	0.050 ± 0.011
Inclination	i	°	86.10 ± 0.61	87.9 ± 1.6	87.48 ± 2.83
RV-curve semi-amplitude	$K_{\rm A}$	m s^{-1}	–	60.8 ± 3.8	–
Barycentric RV	γ	km s^{-1}	-26.532 ± 0.021	–	–
Projected spin–orbit angle	λ	°	-129 ± 17	–	–